PROCEEDINGS OF SCIENCE

The IceCube Neutrino Observatory

Contributions to ICRC 2017 Part IV: Searches for Beyond the Standard Model Physics

arXiv:1710.01197v1 [astro-ph.HE] 3 Oct 2017

Contents

1 **Delayed light emission to distinguish astrophysical neutrino flavors in IceCube —** PoS(ICRC2017)1008 **6**

2 **Search for Signatures of Heavy Decaying Dark Matter with IceCube** PoS(ICRC2017)923 **14**

3 **Latest results and sensitivities for solar dark matter searches with IceCube** PoS(ICRC2017)912 **22**

4 **Searches for annihilating dark matter in the Milky Way halo with IceCube** PoS(ICRC2017)906 **30**

5 **Searches for Dark Matter in the center of the Earth with the IceCube detector —** PoS(ICRC2017)896 **38**

6 **Measurement of water luminescence – a new detection method for neutrino telescopes —** PoS(ICRC2017)1060 **46**

7 **Combined Search for Neutrinos from Dark Matter Annihilation in the Galactic Center using IceCube and ANTARES —** PoS(ICRC2017)911 **54**

35th International Cosmic Ray Conference — ICRC2017
10–20 July, 2017
Bexco, Busan, Korea

© Copyright owned by the author(s) under the terms of the Creative Commons Attribution-NonCommercial-NoDerivatives 4.0 International License (CC BY-NC-ND 4.0).

IceCube Collaboration Member List

M. G. Aartsen[2], M. Ackermann[52], J. Adams[16], J. A. Aguilar[12], M. Ahlers[20], M. Ahrens[44], I. Al Samarai[25], D. Altmann[24], K. Andeen[33], T. Anderson[49], I. Ansseau[12], G. Anton[24], C. Argüelles[14], J. Auffenberg[1], S. Axani[14], H. Bagherpour[16], X. Bai[41], J. P. Barron[23], S. W. Barwick[27], V. Baum[32], R. Bay[8], J. J. Beatty[18,19], J. Becker Tjus[11], K.-H. Becker[51], S. BenZvi[43], D. Berley[17], E. Bernardini[52], D. Z. Besson[28], G. Binder[9,8], D. Bindig[51], E. Blaufuss[17], S. Blot[52], C. Bohm[44], M. Börner[21], F. Bos[11], D. Bose[46], S. Böser[32], O. Botner[50], J. Bourbeau[31], F. Bradascio[52], J. Braun[31], L. Brayeur[13], M. Brenzke[1], H.-P. Bretz[52], S. Bron[25], J. Brostean-Kaiser[52], A. Burgman[50], T. Carver[25], J. Casey[31], M. Casier[13], E. Cheung[17], D. Chirkin[31], A. Christov[25], K. Clark[29], L. Classen[36], S. Coenders[35], G. H. Collin[14], J. M. Conrad[14], D. F. Cowen[49,48], R. Cross[43], M. Day[31], J. P. A. M. de André[22], C. De Clercq[13], J. J. DeLaunay[49], H. Dembinski[37], S. De Ridder[26], P. Desiati[31], K. D. de Vries[13], G. de Wasseige[13], M. de With[10], T. DeYoung[22], J. C. Díaz-Vélez[31], V. di Lorenzo[32], H. Dujmovic[46], J. P. Dumm[44], M. Dunkman[49], B. Eberhardt[32], T. Ehrhardt[32], B. Eichmann[11], P. Eller[49], P. A. Evenson[37], S. Fahey[31], A. R. Fazely[7], J. Felde[17], K. Filimonov[8], C. Finley[44], S. Flis[44], A. Franckowiak[52], E. Friedman[17], T. Fuchs[21], T. K. Gaisser[37], J. Gallagher[30], L. Gerhardt[9], K. Ghorbani[31], W. Giang[23], T. Glauch[1], T. Glüsenkamp[24], A. Goldschmidt[9], J. G. Gonzalez[37], D. Grant[23], Z. Griffith[31], C. Haack[1], A. Hallgren[50], F. Halzen[31], K. Hanson[31], D. Hebecker[10], D. Heereman[12], K. Helbing[51], R. Hellauer[17], S. Hickford[51], J. Hignight[22], G. C. Hill[2], K. D. Hoffman[17], R. Hoffmann[51], B. Hokanson-Fasig[31], K. Hoshina[31,a], F. Huang[49], M. Huber[35], K. Hultqvist[44], M. Hünnefeld[21], S. In[46], A. Ishihara[15], E. Jacobi[52], G. S. Japaridze[5], M. Jeong[46], K. Jero[31], B. J. P. Jones[4], P. Kalaczynski[1], W. Kang[46], A. Kappes[36], T. Karg[52], A. Karle[31], U. Katz[24], M. Kauer[31], A. Keivani[49], J. L. Kelley[31], A. Kheirandish[31], J. Kim[46], M. Kim[15], T. Kintscher[52], J. Kiryluk[45], T. Kittler[24], S. R. Klein[9,8], G. Kohnen[34], R. Koirala[37], H. Kolanoski[10], L. Köpke[32], C. Kopper[23], S. Kopper[47], J. P. Koschinsky[1], D. J. Koskinen[20], M. Kowalski[10,52], K. Krings[35], M. Kroll[11], G. Krückl[32], J. Kunnen[13], S. Kunwar[52], N. Kurahashi[40], T. Kuwabara[15], A. Kyriacou[2], M. Labare[26], J. L. Lanfranchi[49], M. J. Larson[20], F. Lauber[51], D. Lennarz[22], M. Lesiak-Bzdak[45], M. Leuermann[1], Q. R. Liu[31], L. Lu[15], J. Lünemann[13], W. Luszczak[31], J. Madsen[42], G. Maggi[13], K. B. M. Mahn[22], S. Mancina[31], R. Maruyama[38], K. Mase[15], R. Maunu[17], F. McNally[31], K. Meagher[12], M. Medici[20], M. Meier[21], T. Menne[21], G. Merino[31], T. Meures[12], S. Miarecki[9,8], J. Micallef[22], G. Momenté[32], T. Montaruli[25], R. W. Moore[23], M. Moulai[14], R. Nahnhauer[52], P. Nakarmi[47], U. Naumann[51], G. Neer[22], H. Niederhausen[45], S. C. Nowicki[23], D. R. Nygren[9], A. Obertacke Pollmann[51], A. Olivas[17], A. O'Murchadha[12], T. Palczewski[9,8], H. Pandya[37], D. V. Pankova[49], P. Peiffer[32], J. A. Pepper[47], C. Pérez de los Heros[50], D. Pieloth[21], E. Pinat[12], M. Plum[33], P. B. Price[8], G. T. Przybylski[9], C. Raab[12], L. Rädel[1], M. Rameez[20], K. Rawlins[3], I. C. Rea[35], R. Reimann[1], B. Relethford[40], M. Relich[15], E. Resconi[35], W. Rhode[21], M. Richman[40], S. Robertson[2], M. Rongen[1], C. Rott[46], T. Ruhe[21], D. Ryckbosch[26], D. Rysewyk[22], T. Sälzer[1], S. E. Sanchez Herrera[23], A. Sandrock[21], J. Sandroos[32], S. Sarkar[20,39], S. Sarkar[23], K. Satalecka[52], P. Schlunder[21], T. Schmidt[17], A. Schneider[31], S. Schoenen[1], S. Schöneberg[11], L. Schumacher[1], D. Seckel[37], S. Seunarine[42], J. Soedingrekso[21], D. Soldin[51], M. Song[17], G. M. Spiczak[42],

C. Spiering[52], J. Stachurska[52], M. Stamatikos[18], T. Stanev[37], A. Stasik[52], J. Stettner[1], A. Steuer[32], T. Stezelberger[9], R. G. Stokstad[9], A. Stößl[15], N. L. Strotjohann[52], G. W. Sullivan[17], M. Sutherland[18], I. Taboada[6], J. Tatar[9,8], F. Tenholt[11], S. Ter-Antonyan[7], A. Terliuk[52], G. Tešić[49], S. Tilav[37], P. A. Toale[47], M. N. Tobin[31], S. Toscano[13], D. Tosi[31], M. Tselengidou[24], C. F. Tung[6], A. Turcati[35], C. F. Turley[49], B. Ty[31], E. Unger[50], M. Usner[52], J. Vandenbroucke[31], W. Van Driessche[26], N. van Eijndhoven[13], S. Vanheule[26], J. van Santen[52], M. Vehring[1], E. Vogel[1], M. Vraeghe[26], C. Walck[44], A. Wallace[2], M. Wallraff[1], F. D. Wandler[23], N. Wandkowsky[31], A. Waza[1], C. Weaver[23], M. J. Weiss[49], C. Wendt[31], J. Werthebach[21], S. Westerhoff[31], B. J. Whelan[2], S. Wickmann[1], K. Wiebe[32], C. H. Wiebusch[1], L. Wille[31], D. R. Williams[47], L. Wills[40], M. Wolf[31], J. Wood[31], T. R. Wood[23], E. Woolsey[23], K. Woschnagg[8], D. L. Xu[31], X. W. Xu[7], Y. Xu[45], J. P. Yanez[23], G. Yodh[27], S. Yoshida[15], T. Yuan[31], M. Zoll[44]

[1]III. Physikalisches Institut, RWTH Aachen University, D-52056 Aachen, Germany
[2]Department of Physics, University of Adelaide, Adelaide, 5005, Australia
[3]Dept. of Physics and Astronomy, University of Alaska Anchorage, 3211 Providence Dr., Anchorage, AK 99508, USA
[4]Dept. of Physics, University of Texas at Arlington, 502 Yates St., Science Hall Rm 108, Box 19059, Arlington, TX 76019, USA
[5]CTSPS, Clark-Atlanta University, Atlanta, GA 30314, USA
[6]School of Physics and Center for Relativistic Astrophysics, Georgia Institute of Technology, Atlanta, GA 30332, USA
[7]Dept. of Physics, Southern University, Baton Rouge, LA 70813, USA
[8]Dept. of Physics, University of California, Berkeley, CA 94720, USA
[9]Lawrence Berkeley National Laboratory, Berkeley, CA 94720, USA
[10]Institut für Physik, Humboldt-Universität zu Berlin, D-12489 Berlin, Germany
[11]Fakultät für Physik & Astronomie, Ruhr-Universität Bochum, D-44780 Bochum, Germany
[12]Université Libre de Bruxelles, Science Faculty CP230, B-1050 Brussels, Belgium
[13]Vrije Universiteit Brussel (VUB), Dienst ELEM, B-1050 Brussels, Belgium
[14]Dept. of Physics, Massachusetts Institute of Technology, Cambridge, MA 02139, USA
[15]Dept. of Physics and Institute for Global Prominent Research, Chiba University, Chiba 263-8522, Japan
[16]Dept. of Physics and Astronomy, University of Canterbury, Private Bag 4800, Christchurch, New Zealand
[17]Dept. of Physics, University of Maryland, College Park, MD 20742, USA
[18]Dept. of Physics and Center for Cosmology and Astro-Particle Physics, Ohio State University, Columbus, OH 43210, USA
[19]Dept. of Astronomy, Ohio State University, Columbus, OH 43210, USA
[20]Niels Bohr Institute, University of Copenhagen, DK-2100 Copenhagen, Denmark
[21]Dept. of Physics, TU Dortmund University, D-44221 Dortmund, Germany
[22]Dept. of Physics and Astronomy, Michigan State University, East Lansing, MI 48824, USA
[23]Dept. of Physics, University of Alberta, Edmonton, Alberta, Canada T6G 2E1
[24]Erlangen Centre for Astroparticle Physics, Friedrich-Alexander-Universität Erlangen-Nürnberg,

D-91058 Erlangen, Germany
[25]Département de physique nucléaire et corpusculaire, Université de Genève, CH-1211 Genève, Switzerland
[26]Dept. of Physics and Astronomy, University of Gent, B-9000 Gent, Belgium
[27]Dept. of Physics and Astronomy, University of California, Irvine, CA 92697, USA
[28]Dept. of Physics and Astronomy, University of Kansas, Lawrence, KS 66045, USA
[29]SNOLAB, 1039 Regional Road 24, Creighton Mine 9, Lively, ON, Canada P3Y 1N2
[30]Dept. of Astronomy, University of Wisconsin, Madison, WI 53706, USA
[31]Dept. of Physics and Wisconsin IceCube Particle Astrophysics Center, University of Wisconsin, Madison, WI 53706, USA
[32]Institute of Physics, University of Mainz, Staudinger Weg 7, D-55099 Mainz, Germany
[33]Department of Physics, Marquette University, Milwaukee, WI, 53201, USA
[34]Université de Mons, 7000 Mons, Belgium
[35]Physik-department, Technische Universität München, D-85748 Garching, Germany
[36]Institut für Kernphysik, Westfälische Wilhelms-Universität Münster, D-48149 Münster, Germany
[37]Bartol Research Institute and Dept. of Physics and Astronomy, University of Delaware, Newark, DE 19716, USA
[38]Dept. of Physics, Yale University, New Haven, CT 06520, USA
[39]Dept. of Physics, University of Oxford, 1 Keble Road, Oxford OX1 3NP, UK
[40]Dept. of Physics, Drexel University, 3141 Chestnut Street, Philadelphia, PA 19104, USA
[41]Physics Department, South Dakota School of Mines and Technology, Rapid City, SD 57701, USA
[42]Dept. of Physics, University of Wisconsin, River Falls, WI 54022, USA
[43]Dept. of Physics and Astronomy, University of Rochester, Rochester, NY 14627, USA
[44]Oskar Klein Centre and Dept. of Physics, Stockholm University, SE-10691 Stockholm, Sweden
[45]Dept. of Physics and Astronomy, Stony Brook University, Stony Brook, NY 11794-3800, USA
[46]Dept. of Physics, Sungkyunkwan University, Suwon 440-746, Korea
[47]Dept. of Physics and Astronomy, University of Alabama, Tuscaloosa, AL 35487, USA
[48]Dept. of Astronomy and Astrophysics, Pennsylvania State University, University Park, PA 16802, USA
[49]Dept. of Physics, Pennsylvania State University, University Park, PA 16802, USA
[50]Dept. of Physics and Astronomy, Uppsala University, Box 516, S-75120 Uppsala, Sweden
[51]Dept. of Physics, University of Wuppertal, D-42119 Wuppertal, Germany
[52]DESY, D-15738 Zeuthen, Germany
[a]Earthquake Research Institute, University of Tokyo, Bunkyo, Tokyo 113-0032, Japan

Acknowledgment: The authors gratefully acknowledge the support from the following agencies and institutions: USA - U.S. National Science Foundation-Office of Polar Programs, U.S. National Science Foundation-Physics Division, University of Wisconsin Alumni Research Foundation, the Center for High Throughput Computing (CHTC) at the University of Wisconsin - Madison, the Open Science Grid (OSG) grid infrastructure and the Extreme Science and Engineering Discovery Environment (XSEDE); U.S. Department of Energy, and National Energy Research Scientific Computing Center; Particle Astrophysics research computing center at the University of Maryland; Institute for Cyber-Enabled Research at Michigan State University; Astroparticle Physics Computational Facility at Marquette University; Belgium - Funds for Scientific Research (FRS-FNRS and FWO), FWO Odysseus and Big Science programs, Belgian Federal Science Policy Office (Belspo); Germany - Bundesministerium für Bildung und Forschung (BMBF), Deutsche Forschungsgemeinschaft (DFG), Helmholtz Alliance for Astroparticle Physics (HAP), Initiative and Networking Fund of the Helmholtz Association; Deutsches Elektronen Synchrotron (DESY); Cluster of Excellence (PRISMA ? EXC 1098); High Performance Computing Cluster of the IT-Center of the RWTH Aachen; Sweden - Swedish Research Council, Swedish Polar Research Secretariat, Swedish National Infrastructure for Computing (SNIC), and Knut and Alice Wallenberg Foundation; Canada - Natural Sciences and Engineering Research Council of Canada, Calcul Québec, Compute Ontario, WestGrid and Compute Canada; Denmark - Villum Fonden, Danish National Research Foundation (DNRF); New Zealand - Marsden Fund, New Zealand; Australian Research Council; Japan - Japan Society for Promotion of Science (JSPS) and Institute for Global Prominent Research (IGPR) of Chiba University; Korea - National Research Foundation of Korea (NRF); Switzerland - Swiss National Science Foundation (SNSF).

PROCEEDINGS OF SCIENCE

Delayed light emission to distinguish astrophysical neutrino flavors in IceCube

The IceCube Collaboration
http://icecube.wisc.edu/collaboration/authors/icrc17_icecube

E-mail: ansteuer@uni-mainz.de, lutz.koepke@uni-mainz.de

IceCube, a cubic kilometer Cherenkov detector, is an ideal instrument for the detection of astrophysical neutrino fluxes and rare interactions of exotic particles. One way to advance IceCube neutrino analyses would be the development of methods to identify the neutrino flavor and reaction type. While charged current interactions leading to long tracks of charged muons can be easily distinguished from those leading to particle cascades of $\mathcal{O}(10\,\mathrm{m})$ extension, the 17 m sensor distance makes it very challenging to identify the type of cascade as being due to the fragmentation of the struck nucleus or due to showers initiated by electrons or tauons. Only at very high energies, the average τ flight distance of 50 m/PeV, in principle, allows one to identify a ν_τ interaction. So far, IceCube has not registered telltale events of such kind.
The creation of neutrons, spallation products and muons in hadronic showers offers an alternative handle to identify a hadronic interaction. However, the regular data acquisition system is restricted to a $\mathcal{O}(10\,\mu\mathrm{s})$ readout window, limiting the detection to relativistic or low relativistic particles. Recently, the development of a spooling system to store the complete detector hit map for a configurable time interval made it possible to register a potential "afterglow" of highly energetic events. While the signal from Michel electrons from muon decay will be difficult to extract due to light scattering in the ice and afterpulses of the PMTs, the detection of 2.224 MeV photons from neutron capture on hydrogen is promising due to the low PMT dark rates of the sensors in IceCube. One should note that luminescence in the ice could be a competing effect.
In this paper, we summarize the physics scope and particle identification opportunities, study the underlying physics of delayed signals and the expected detector response in a Cherenkov detector, discuss a newly installed automatic real time triggering system, with emphasis on the the capabilities and limitations of the data acquisition system for such an analysis, and outline the expected potential of IceCube for particle identification through the use of delayed signals.

Corresponding author: A. Steuer* and L. Köpke
Johannes Gutenberg University Mainz, Germany

35th International Cosmic Ray Conference -ICRC217-
10-20 July, 2017
Bexco, Busan, Korea

*Speaker.

PoS(ICRC2017)1008

1. Delayed light emission processes and physics scope of cascade identification

The striking background reduction by the coincident registration of a delayed neutron signal was vital for the first detection of $\bar{\nu}_e$ in the 1956 neutrino discovery experiment by Cowan and Reines. Since then, many experiments have been relying on characteristic delayed signals to identify rare neutrino interactions in the presence of large backgrounds. The possible use of delayed signals in IceCube [1] for flavor-identification was pointed out in a recent paper by S. Li, M. Bustamante and J.F. Beacom [2], which stimulated the ongoing efforts in IceCube. The detection of Michel electrons from muon decay is challenging due to light scattering in the ice and the occurrence of afterpulses. Spallation products, such as those from the decay of ^{16}N or ^{12}B nuclei, contribute less than 1% to delayed signals. In this note, we therefore concentrate on the detection of the "neutron echo". Before being captured, the neutrons are moderated by elastic scattering and the number of neutrons dN captured in a time interval dt is given by $dN \propto -N\sigma v dt \propto -N\lambda dt$, with $\sigma \propto 1/v$. Hence, one observes an exponential time dependence of the capture process. In ice, the effective moderation time constant $\tau_m = 1/\lambda$ amounts to $\tau_m \approx 190\,\mu$s, with a spread of $\approx 18\,\mu$s from hadronic shower fluctuations. Signals from neutron capture were measured by Super-Kamiokande in water, both with a neutron source and cosmic ray muons [3, 4] and confirm these simulation results.

When deciphering the origin of astrophysical neutrinos, their flavor composition plays a similarly important role as their direction and energy dependence. A flavor composition at the source of $(\frac{\nu_e}{\nu_{total}} : \frac{\nu_\mu}{\nu_{total}} : \frac{\nu_\tau}{\nu_{total}}) = (\frac{1}{3} : \frac{2}{3} : 0)$, expected for pion decay, is transformed by incoherent neutrino vacuum mixing to approximately $(\frac{1}{3} : \frac{1}{3} : \frac{1}{3})$ at Earth, providing a large fraction of τ neutrinos through oscillation. As can be seen from Fig. 1 (left), present data have little power to separate ν_e from ν_τ initiated showers. Methods to experimentally separate these contributions are therefore needed. In IceCube, a positive ν_τ identification has not yet occurred (see e.g. [5, 6]). A further flavor

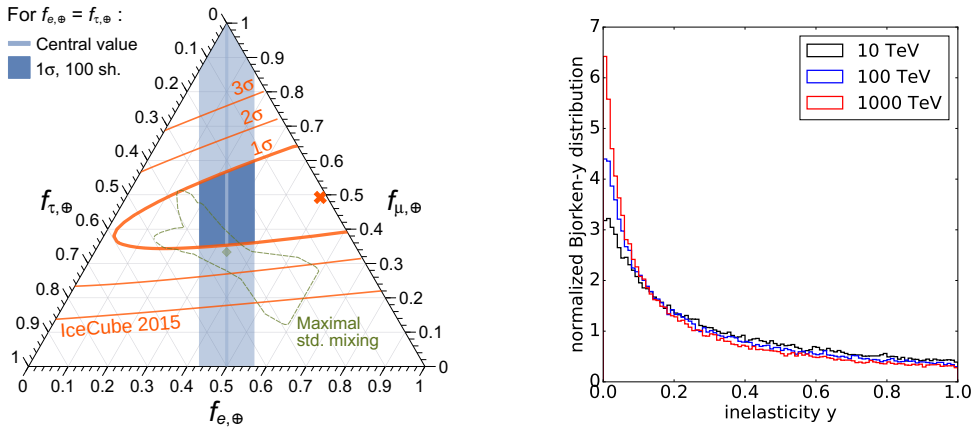


Figure 1: Left: Flavor composition $f_l (l = e, \mu, \tau)$ of astrophysical neutrinos at Earth. Read each axis parallel to its respective ticks. Orange: IceCube fit [7], blue: prediction by [2] assuming 100 showers of 100 TeV under ideal conditions for delayed photon observation, green: allowed range by current mixing uncertainties. Right: normalized y-distributions for $E_\nu = 10$, 100 and 1000 TeV using the parametrization of [8].

sensitive category of events are $\bar{\nu}_e$ reacting on e^- in the electronic clouds of ice molecules, thereby creating on-shell W^- bosons. The resonant reaction leads to a peak in the neutrino cross section at around 6.3 PeV ("Glashow resonance"). IceCube should be on the verge of detecting such events

PoS(ICRC2017)1008

if the spectrum is not cut off at high energies. As the W^- decays to hadrons 69.8% of the time, including hadronic τ decays, their identification as being hadronic would sharpen the interpretation as being due to the Glashow resonance.

A neutrino interacts with a nucleon N via the charged current reaction $\nu_l + N \to l + X$ or the neutral-current channel $\nu_l + N \to \nu_l + X$, where l =e, μ or τ and X represents hadrons produced in the fragmentation of the target nuclei. The distribution of the energy fraction y ("inelasticity") carried by final-state hadrons peaks at $y = 0$ with a long tail towards higher y-values; the average decreases with energy, yielding e.g. $< y > \approx 0.3$ for 100 TeV ν and $\bar{\nu}$ interactions (see Fig. 1 right).

For a given reconstructed event energy in the detector, the contribution of neutral current interactions of all flavors depends on the assumed spectral index and on the ν energy, as the inelasticity distribution is peaked at low values and the neutrino spectrum is steeply falling ($\approx$ 7% neutral current contribution for $\gamma = 2.6$ and 100 TeV detected energy). An excess of high energy hadronic showers would therefore be an intriguing indication of unexpected physics.

Long tracks are produced by ν_μ charged current interactions and, in 17% of the cases, in $\tau \to \mu \nu_\mu \nu_\tau$ decays. Approximately 65% of the τ leptons decay hadronically with $\approx$ 25% of the energy escaping undetected by neutrinos. In the case of charged current ν_e interactions, electron- and hadron initiated showers combine approximately to the total neutrino energy with fractions determined by the inelasticity distribution.

There are many possibilities to explore beyond the Standard Model physics if one could distinguish between hadronic, tauonic and electromagnetic showers. As can be seen from Fig. 1 (left), the allowed range for standard neutrino mixing for different production scenarios is rather restricted. Therefore the flavor composition analysis could be an interesting indicator of new physics. Similarly, neutrino cross sections above 1 TeV have never been probed experimentally.

The IceCube excess of neutrinos exceeding 100 TeV energy has led to much speculation with regards to their origin, including top down scenarios. For example, it has been argued that the observed spectrum is indicative for the interaction of boosted dark matter, where a very heavy dark matter particle decays and thereby produces a strongly boosted secondary particle that triggers a nuclear recoil in the IceCube detector [9, 10]. As such a recoil would be completely hadronic in nature and the natural occurrence of neutral current interactions is rare, such a scenario could be immediately tested if the shower-type information were available.

2. Shower development, physics of delayed signals and detector response

Electromagnetic showers start out with electrons, positrons and gamma rays and only few pions and nucleons are subsequently produced by photo-nuclear processes. A hadronic shower starts out with mesons and nucleons, building up a progressively larger fraction of electromagnetic particles from prompt $\pi^0 \to \gamma\gamma$ decays. The shower development ends once energy-loss processes dominate the particle production. At this stage, pions contribute $\approx$ 10% to the Cherenkov light in hadronic showers and less than 1% in electromagnetic showers. Evaporated neutrons are characteristic of hadronic showers and are mostly absent in electromagnetic showers. Neutrons with MeV energies thermalize by undergoing a random walk until they are captured on hydrogen forming an excited deuteron that subsequently decays with the emission of a 2.224 MeV photon. At the end of the shower development, π^- are typically captured by nuclei after coming to rest by

PoS(ICRC2017)1008

ionization. π^+ decay to μ's which subsequently, after decaying with an average lifetime of 2.2 μs, produce positrons with $\approx$ 35 MeV energy. Note that the Cherenkov yields from hadronic and electromagnetic interactions are not identical but close at high energies, as the electromagnetic fraction in hadronic showers rises from ≈75% at 1 TeV to ≈92% at 1 PeV. As a consequence, the relative number of Cherenkov photons seen in a hadronic shower compared to a purely electromagnetic shower reaches 94% at 1 PeV energy (see Fig. 2).

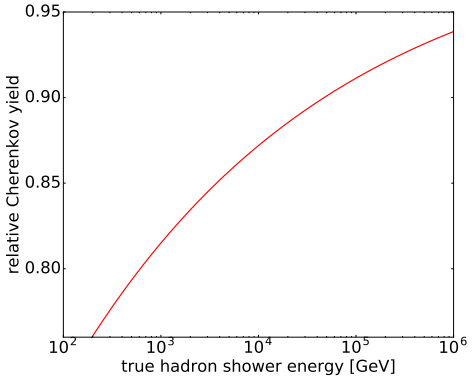


Figure 2: Cherenkov photon yield from hadronic showers relative to electromagnetic showers (Pythia particle spectra plus Geant4 hadronic showers [11]).

2.1 Pythia and Geant4 simulation without detector response

The deep inelastic scattering of ν's of all species on protons has been simulated in Pythia 8 including the DIRE-plug-in [12] to implement all order radiative corrections using a dipole re-summation technique. All final state particles with their kinematic information are then written to files that can be read by Geant4 and the standard IceCube simulation. Geant4 is then used in CPU-intensive simulations of particles in natural ice[1]. The number of delayed photons due to neutron capture and the total number of Cherenkov photons are stored for each particle type and energy. Parametrized results are then provided to a fast simulation. The sensitivity to Geant4's hadronic models (physics lists) and cuts has been investigated and a comparison to a FLUKA calculation [2] has been performed. The predicted strength of the neutron capture signal varies by ≈ 40%, however, the uncertainty may be even larger [2].

The result of the pure Geant4 simulation, which disregards detector effects and thus represents the optimal resolution limited only by the shower development, is shown in Fig. 3 (left) as the ratio of the number of neutron capture induced Cherenkov photons over the total photon count. There is a clear separation of shower types seen: charge current ν_e interactions follow the inelasticity distribution in shape and neutral current interactions produce a symmetric Gaussian-like distribution, with on average 0.00055 delayed per prompt photon. The 25% relative spread reflects the fluctuations in the hadron shower. The low τ decay multiplicity and ≈ 25% undetected energy in hadronic τ decays from neutrinos lead to a shift and broadening of the distribution.

In order to quantify the optimal flavor discrimination potential when being limited only by physical fluctuations, we follow Ref. [2] in defining a Bayesian probability that takes into account a hypothesis on the initial flavor ratio and the rareness of neutral current decays. A Bayesian approach is useful in the view of combining particle identification measures and to visualize systematic dependencies. Figure 3 (right) shows the expected reaction discrimination potential for the assumption of an equal partition of flavors between astrophysical neutrinos. The discrimination improves slightly with rising energy due to the tightening of the inelasticity distribution (not shown). The band indicates the dependence on the assumption of the spectral index. Clearly, the distribution

[1] The ice is assumed to be made up of 89.7% $^1H_2^{16}O$, 0.2% $^1H_2^{18}O_2$, 0.03% $^1H^2H^{16}O$ as well as ≈ 10% of natural air, whith contributions given in volume percent.

PoS(ICRC2017)1008

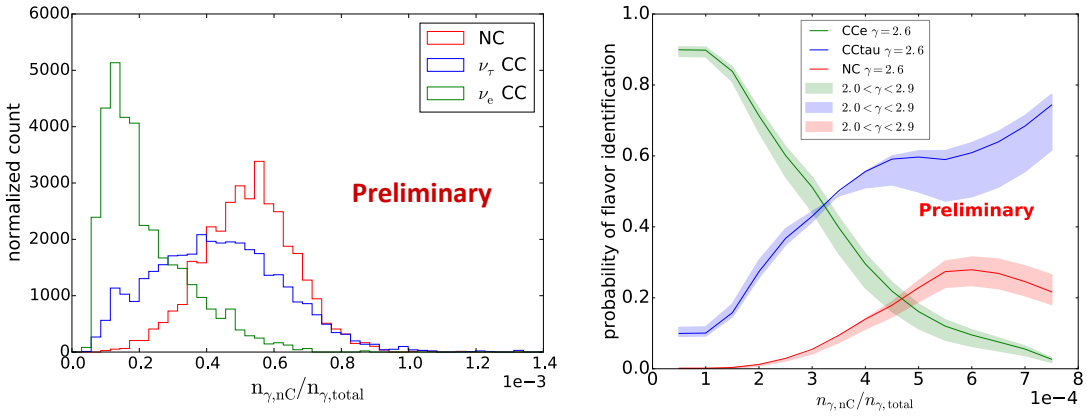


Figure 3: Left: Geant4 result on the ratio of neutron capture induced and total Cherenkov photons. Right: Bayesian shower identification probability according to [2] (Appendix A), assuming neutrino flavor equipartition, 100 TeV detected energy and a range in spectral indexes.

is sensitive to the flux assumption and would look very different when e.g. assuming the expected ratio of atmospheric neutrinos or prompt neutrinos from charm. In order to determine a possible "new physics" contribution, we will choose a frequentist approach and compare the data to the null hypothesis of a standard event decompositon.

2.2 IceCube simulation

The events generated by Pythia and DIRE were interfaced with the Geant4 based version of the IceCube Monte Carlo and processed to detection level, including a likelihood based energy reconstruction [13] for cascades. Because the CPU time rises strongly with energy, we restricted ourselves to neutrino interactions with reconstructed energies between 100-150 TeV. In Fig. 4 we show the IceCube per event response to delayed photons in hadron showers. In this particular simulation, the detector noise simulation had been switched off for clarity. While one clearly observes the fall-off due to delayed photons from neutron capture, there is a observable gap between 10-45 μs separating “prompt“ and “delayed“ photons. This behavior is due to deadtime effects in the digitizing electronics which will be described in the following paragraph in detail.

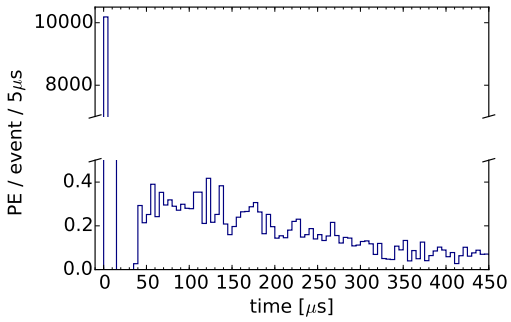


Figure 4: IceCube simulation of neutral current events with registered energies between 100-150 TeV (detected photo electrons (PE) for 5 optical modules with highest signal expectation).

2.3 Deadtime effects of the electronics

In IceCube, Cherenkov photons emitted from charged particles are detected by 25.4 cm diameter photomultipliers which amplify the charge of the recorded PE by roughly a factor of 10^7. These signals are stored by tandem ATWDs with 300 MHz sampling rate for $\approx$ 427 ns and are digitized and transmitted afterwards [1]. Each ATWD has 3 input channels with factors of 16, 2, and 0.25 amplification in order to increase the 10 bit resolution to effectively 15 bits. An FADC with 10 bit

PoS(ICRC2017)1008

resolution and 40 MHz sampling rate can record up to 6.4 μs. The combination of ATWDs and an FADC allows for a nearly deadtime free recording of prompt particle interactions including delays that photons suffer from scattering in the ice. However, when extending the readout to much larger time spans, several deadtime effects start impacting the data taking due to the digitization process [2]. Obviously, the deadtime hinges on the number of amplification channels used and therefore strongly depends on the shower position and energy (see Fig. 5 right). Often, afterpulses start the second ATWD so that the deadtime can occur after some delay and introduces a complex repetitive pattern.

In order to acquire the necessary statistics to smoothen the deadtime probability density distribution for the later use in a likelihood fit, a fast code was implemented to simulate the photon propagation, afterpulses and the electronics response. Figure 5 shows an example of the deadtime effect in the five optical modules with the highest signal expectation as function of time. This result for a 750 TeV shower was obtained from the high statistics simulation discussed above.

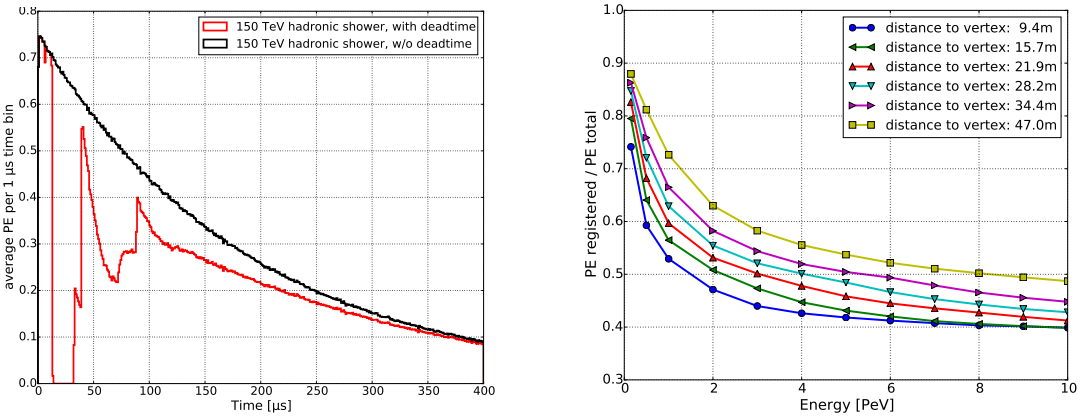


Figure 5: Left: example for the effect of the deadtime on an event with 150 TeV shower energy averaged over five optical modules with distances to the shower vertex between 15.4 m and 40.3 m. Right: overall loss of registered PEs due to deadtime as function of energy and shower vertex distance to the closest optical module.

3. High energy starting events, real time filtering and HitSpool data acquisition

In 2013, IceCube reported the discovery of an astrophysical flux of neutrinos in the 60 TeV to multiple PeV energy range [14]. The key to this discovery was a focus on events in which the neutrino vertex is contained in a fiducial volume that covers slightly less than half of IceCube. The outer surface of the detector is used to reject events with the signature of atmospheric μ's and ν's and a requirement of at least 1500 detected PEs is imposed. Below 6000 PEs, 95 % of the events are due to atmospheric muons that are nor tagged by the veto layers. The high energy starting event analysis therefore concentrates on events with > 6000 PEs, roughly equivalent to a minimal energy of 30 TeV, with an estimated background of atmospheric neutrinos and muons of roughly 17% and 23%, respectively [15]. Cascades signatures dominate the sample.

[2] The recording on ATWDs and FADC is blocked by $\Delta t = t_{\text{reset}} + t_{\text{DAQ}} + t_{\text{clear}} \cdot (4-n) + t_{\text{readout}} \cdot n < 88.6\,\mu$s, with $n \in \{1,2,3\}$ being the number of ATWD input channels involved. Reset, data taking, clearing and readout times are given by $t_{\text{reset}} = 225$ ns, $t_{\text{DAQ}} = 426.67$ ns, $t_{\text{clear}} = 950$ ns, and $t_{\text{readout}} = 29$ ns.

PoS(ICRC2017)1008

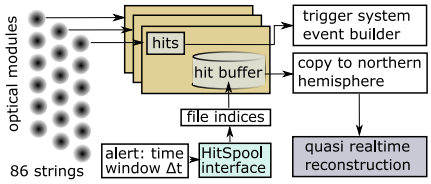


Figure 6: Data flow for saving the detector hit image (HitSpooling) for $\Delta t = 1$ s.

The high energy starting event sample is well understood, is automatically selected by a filter script at South Pole with a median latency of ≈ 40 s, is of sufficiently small size and thus very well suited for the analysis described in this note. In order to provide access to all hits independent of the time of a trigger, the hit stream from each optical module is buffered in a dedicated industrial computer, where the hits are chronologically ordered and packaged. A copy of the raw data is written (see Fig. 6) to a circular buffer on disk (HitSpool [1]). In the case of a high energy starting event candidate with > 1500 registered photoelectrons (PE), a request is sent to the HitSpool system to store hits within 1 s of the trigger and to initiate an automatic transfer of data to the North and the subsequent processing. The system has been working reliably since February 2016. The automatic processing models the triggers, removes backgrounds, reconstructs energies and provides various file formats to the user. As of April 2017, 1270 events have been registered, with around 20 events in a blinded region above 6000 PE. Analyzing the five optical modules with the highest photon count expectation and subtracting the average estimated dark count background (≈ 0.0006 hits per μs), the distribution in Fig. 7 shows clear evidence for delayed hits for $t > 50\,\mu$s. In fact, the signal is surprisingly large, given the dominance of atmospheric muons (95%) in the sample. An explanation may be that the background is dominated by catastrophic energy losses, $\approx$ 15% of which have a photonuclear origin. A quantitative study is on its way.
In order to optimally extract the signal in the presence of dark noise, one can go one step further and use a likelihood approach. The likelihood

$$L(n_s) = \frac{\exp(-\mu_b)\cdot\mu_b}{\Gamma(N-n_s+1)} \prod_{j=1}^{N_{\mathrm{HIT}}} \prod_{i=1}^{N_{\mathrm{DOM}}} \left(\frac{n_s}{N} \cdot P_{s(i,j)}(\vec{r},t) + \frac{N-n_s}{N} \cdot P_b \right) \tag{3.1}$$

exploits the expected temporal distribution and the expected position dependent energy deposition of the signal.

In equation 3.1, n_s denotes the number of delayed photons, N is the number of all registered photons, $\mu_b \approx 0.55 \cdot N_{\mathrm{DOM}}$ is the expected number of dark counts and N_{DOM} is the number of optical modules taken into account in the fit with N_{HIT} hits per optical module. The signal probability $P_{s(i,j)}(\vec{r},t) = P_{s(i,j)}(\vec{r}) \cdot P_{s(i,j)}(t)$ can be factorized in a spacial part $P_{s(i,j)}(\vec{r}) = q_i / (\sum_{i=1}^{N_{\mathrm{DOM}}} q_i)$ and a temporal part $P_{s(i,j)}(t_j) = \frac{f_{\mathrm{dt}}}{\tau} \exp(-t_j/\tau)$, with the expected number of photons per DOM q_i, the neutron moderation time $\tau = 190\,\mu$s and the time and position dependent deadtime correction f_{dt}. $P_b \approx 1/N_{\mathrm{DOM}} \cdot 1/\Delta t$ is the uniform background hypothesis

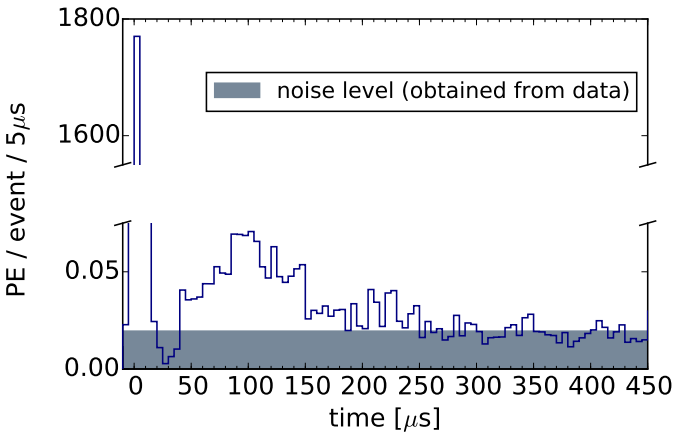


Figure 7: Stacked time distribution for 1250 high energy starting events with 1500-6000 PE recorded.

PoS(ICRC2017)1008

for an analysis period $\Delta t \approx 1$ ms. A toy Monte Carlo study showed that deposited hadronic energies larger than ≈ 100 TeV are required to obtain a significant result on the fraction of delayed photons and that statistical uncertainties better than 25 % will be achieved if the hadronic energy exceeds 500 TeV. Including more than $N_{\mathrm{DOM}} = 15$ optical modules in the likelihood fit will not significantly improve the results.

4. Summary

Delayed signals in neutrino reactions may be used to classify electromagnetic, hadronic and tau induces showers and thus provide a potential tool to determine the neutrino flavor composition and to test the data for unexpected phenomena. Preliminary Monte Carlo studies of the IceCube response to delayed photons from neutron capture indicate that the method becomes sensitive if hadronic energies exceed ≈ 100 TeV. A search in an atmospheric muon dominated, real-time extracted data set shows clear evidence for such delayed processes. If alternative sources [16] can be excluded and if large uncertainties in the simulation of hadronic processes can be reduced [17] and dead time effects are properly handled, the method will provide a complimentary flavor discrimination tool in the future.

References

[1] **IceCube** Collaboration, M. G. Aartsen et al., *JINST* **12** (2017) P03012.

[2] S. W. Li, M. Bustamante and J. F. Beacom, [astro-ph.HE/1606.06290].

[3] **Super-Kamiokande** Collaboration, H. Watanabe et al., *Astropart. Phys.* **31** (2009) 320.

[4] **Super-Kamiokande** Collaboration, H. Zhang et al., *Astropart. Phys.* **60** (2015) 41.

[5] **IceCube** Collaboration, M. G. Aartsen et al., *Phys. Rev.* **D** 93, no. 2, 022001 (2016).

[6] **IceCube** Collaboration, PoS(ICRC2017)974 (these proceedings).

[7] **IceCube** Collaboration, M. G. Aartsen et al., *Phys. Rev. Lett.* **114** (2015) 171102.

[8] A. Connolly, R. S. Thorne and D. Waters, *Phys. Rev.* **D83** (2011) 113009.

[9] J. Kopp, J. Liu and X.P. Wang, *JHEP***04** (2015) 105.

[10] A. Bhattacharya, R. Gandhi, A. Gupta and S. Mukhopadhyay, *JCAP* **05** (2017) 002.

[11] L. Rädel, Master's thesis, RWTH Aachen (2012).

[12] S. Höche and S. Prestel, *Eur. Phys. J.* **C75** (2015) 461.

[13] **IceCube** Collaboration, M. G. Aartsen et al., *JINST* **9** (2014) P03009.

[14] **IceCube** Collaboration, M. G. Aartsen et al., *Science* **342** (2013) 1242856.

[15] **IceCube** Collaboration, PoS(ICRC2015)1081 (2016).

[16] **IceCube** Collaboration, PoS(ICRC2017)1060 (these proceedings).

[17] I. Anghel et al., *ANNIE LOI*, [physics.ins-det/1504.01480].

PoS(ICRC2017)1008

PROCEEDINGS OF SCIENCE

Search for Signatures of Heavy Decaying Dark Matter with IceCube

The IceCube Collaboration[†]

[†] *http://icecube.wisc.edu/collaboration/authors/icrc17_icecube*

E-mail: stettner@physik.rwth-aachen.de,
hrvoje.dujmovic@icecube.wisc.edu

Neutrino telescopes provide some of the best sensitivities for heavy decaying dark matter. With IceCube's observation of high-energy astrophysical neutrinos, interest in scenarios that could explain their origin as a result of the decay of long-lived heavy dark matter particles has risen. We present two dedicated experimental analyses to test this scenario of decaying dark matter with masses above 10 TeV. One analysis uses 6 years of IceCube data focusing on muon-neutrino tracks from the northern hemisphere and one analysis uses 2 years of cascade data from the full sky. The following contributions to the neutrino flux are considered: Atmospheric neutrinos, a diffuse astrophysical flux following a power-law spectrum and a potential flux of neutrinos produced in dark matter decays. The latter can be distinguished by its distinctive features in the energy spectrum (cut-off at half the mass of the DM-particle) and asymmetry of the arrival directions due to the DM halo of our galaxy. We present best-fit results and deduce lower lifetime limits on the order of 10^{28}s for dark matter masses above 10 TeV.

Corresponding authors: Jöran Stettner*[1], Hrvoje Dujmovic[2]

[1] *III. Physikalisches Institut, RWTH Aachen University, Germany*

[2] *Dept. of Physics, Sungkyunkwan University, Korea*

35th International Cosmic Ray Conference — ICRC2017
10–20 July, 2017
Bexco, Busan, Korea

*Speaker.

1. PeV-Neutrinos and Dark Matter

To this day, the origin of the high energy neutrino flux discovered by IceCube, with the purely atmospheric contribution being disfavoured at over 5σ [1, 2], remains unidentified [3]. We present two dedicated analyses to test the explanation of heavy ($m > 10\,\mathrm{TeV}$), unstable particles producing neutrinos in their decays as an alternative to bottom-up astrophysical acceleration scenarios. Since such heavy particles are predicted in many models which also aim to describe the particle nature of dark matter [4], the observation of high-energy neutrinos allows us to probe heavy decaying dark matter at the corresponding mass scales.

2. Experimental Data

The IceCube observatory is a cubic-kilometre neutrino detector installed in the ice at the geographic South Pole between depths of 1450 m and 2450 m [5]. Detector construction started in 2005 and finished in 2010. The neutrino reconstruction relies on the optical detection of Cherenkov radiation induced by secondary particles produced in neutrino interactions in the surrounding ice or the nearby bedrock.

For the presented analyses, two different event samples are used: The first analysis is based on six years of muon-neutrino data, i.e. track-like events from the northern hemisphere (no background from atmospheric muons) [2]. This event selection contains data from 2009 to 2014: The first two seasons consist of data taken with the partially installed detector, indicated by the labels IC59 and IC79. The season 2011 is labelled IC86-1 (full configuration) and the last three seasons are summarized as IC86-234 (full configuration and improved simulation). The second analysis uses two years of full-sky starting events. The data was taken during the period of June 2010 to March 2012 during the last year of construction (IC79) and the first year of full detector operation (IC86-1). The event selection is based on a previous study [6] which used a containment cut in order to achieve a high signal purity. In addition, a cut on the event track length is used to select only cascade-like events. These are events induced via an electron or tau neutrino or via a muon neutrino neutral current interaction. Due to the containment cut, the effective volume and thus the expected signal rate of the cascade sample is significantly smaller than that of the track sample. The cascade sample does, however, have a full sky coverage and an improved energy resolution which makes both analysis complementary to each other. The data samples do not share any events and the results can be treated as statistically independent.

	Numer of Events	Years	Sky coverage	Purity
Track Sample	352,294	6y (2009-2014)	Nth. Hemisph. ($\Theta > 85^\circ$)	99.7%
Cascade Sample	278	2y (2010-2012)	Full Sky	90%

Table 1: Summary of the two event samples.

3. Analysis Methods

To test whether the observed flux of high-energy neutrinos (partly) arises from heavy decaying dark matter, a forward folding likelihood fit is performed.

3.1 Flux Components

The flux components contributing to the total flux of neutrinos are of atmospheric and astrophysical origin. For a given neutrino energy and direction, the expected flux is calculated from the sum of the different flux templates.

Background components The largest source of background are conventional atmospheric neutrinos that originate from the decay of pions and kaons in cosmic ray air showers. These neutrinos are the largest background in both the track and the cascade sample. Atmospheric muons are not able to pass through the Earth, so they only contribute to the southern sky background. Another atmospheric background is expected from the prompt decay of charmed mesons, although the flux has not been detected yet [2]. A potential prompt contribution to the flux is therefore taken into account in both analyses as systematic uncertainty. Atmospheric neutrino flux predictions are taken from [7] and [8] for the conventional and prompt component (modified to account for the cosmic-ray knee), respectively.

Astrophysical Background: Cosmic-rays re-interacting in the vicinity of their production sites are expected to produce high-energy neutrinos [9]. A generic description that agrees well with the observed data is a diffuse flux following a single power-law energy spectrum [1, 2]. To allow for deviations from preceding results, the spectral index and the flux normalization are taken as free parameters in the presented analyses.

$$\Phi^{\text{astro.}} = \Phi_0 \times (E_\nu / 100\,\text{TeV})^{-\gamma} \tag{3.1}$$

Signal component Hypothetical heavy dark matter particles may decay into standard model particles (e.g. neutrinos [4]). The exact decay channel depends on the detailed nature of the dark matter particle. In the presented analyses, two similar hard benchmark channels are investigated (line-feature at $E_\nu = m/2$): $DM \to Z^0 + \nu_\tau$ (oscillated into ν_μ) for the analysis using track-like events and $DM \to H^0 + \nu$ (flavour agnostic) for the analysis using the cascade sample, see figure 1. If there is a contribution from decaying dark matter to the high-energy neutrino flux, it can be identified with these benchmark channels. The derived lifetime limits can furthermore be translated to other decay channels.

The total expected flux from the hypothetical decay of dark matter consists of two components which are added up: dark matter particles decaying in the galactic halo and at cosmological distances [10]. Both share the same free model parameters in the fit, namely the lifetime and mass of the hypothetical dark matter particle.

The galactic component is expected to generate a flux of astrophysical neutrinos with two distinct features: An energy distribution which directly follows the decay spectrum $\frac{dN_\nu}{dE_\nu}$ and an angular distribution corresponding to the line-of-sight integral $J(\Psi)$.

$$\frac{dJ^{\text{Halo}}}{dE_\nu} = \frac{1}{4\pi m_{DM}\tau_{DM}} \frac{dN_\nu}{dE_\nu} \times J(\Psi) \qquad J(\Psi) = \int_0^\infty \rho_{DM}(r)\, ds \tag{3.2}$$

The Burkert profile is used as parametrization for the galactic halo with best fit parameters from [11], other halo profiles are studied as systematic uncertainty in Section 4.1. Compared to dark matter annihilation searches, the linear dependency on the dark matter density 3.2 makes the presented analyses less sensitive to the assumed halo profile.

The second dark matter subcomponent is coming from DM particles decaying at cosmological distances. The flux is assumed to be isotropic and the energy distribution follows the red-shifted decay spectrum. Using the ΛCDM model with parameters from [12], the expected flux is calculated from the original decay spectrum and the dark matter density in the universe Ω_{DM}.

$$\frac{dJ^{\text{Cosm.}}}{dE_\nu} = \frac{\Omega_{DM}\rho_{crit.}}{4\pi m_{DM}\tau_{DM}} \int_0^\infty \frac{1}{H(z)} \frac{dN_\nu}{d(E_\nu(1+z))} dz \qquad H(z) = H_0\sqrt{\Omega_\Lambda + \Omega_m(1+z)^3}. \tag{3.3}$$

3.2 Likelihood Fit and Test-Statistic Definition

The likelihood fit aims to disentangle the different flux components by comparing 3d flux templates with the experimental data as a function of energy, zenith angle and right-ascension. The templates are calculated from flux expectations which were obtained from a full detector simulation taking into account the same event selections as used for the experimental data.

The fit is performed by maximizing the Poisson likelihood to observe n events if $\mu(\xi)$ are expected for a given set of fit-parameters ξ. The analysis of track-like events computes the likelihood per bin of $\log_{10}(E_\mu^{\text{reco.}})$, cos(zenith) and right-ascension using Equation 3.4. The analysis of cascade-like events uses the unbinned likelihood (Eq. 3.5) obtained in the limit of an infinite number of bins. N is the total number of observed events and $M = \int \mu \; dEd\Omega$ the total number of expected events.

$$L(N;\xi) = \prod_{i=1}^{bins} \mathrm{P}(n_i;\mu_i(E_j,\phi_j,\theta_j;\xi)) \tag{3.4}$$

$$L(N;\xi) = \frac{\mathrm{P}(N;M)}{M^N} \prod_{j=1}^{N} \mu(E_j,\phi_j,\theta_j;\xi) \tag{3.5}$$

Two fits are performed on the experimental data: The background hypothesis is the atmospheric and a diffuse astrophysical flux, the signal hypothesis additionally allows for a flux from decaying dark matter. Based on the two fits, a test statistic (Eq. 3.6) is calculated from the maximized likelihoods.

$$TS := 2 \times \log\left(\frac{L(\hat{\phi}_{astro},\hat{\gamma},\hat{m},\hat{\tau})}{L(\hat{\phi}_{astro},\hat{\gamma},\tau=\infty)}\right) \geq 0 \tag{3.6}$$

4. Experimental Results and Systematic Uncertainties

The best-fit results are summarized in Table 2: Both show a decrease of the diffuse astrophysical flux if dark matter is considered in the fit (more so in the track analysis). However, the

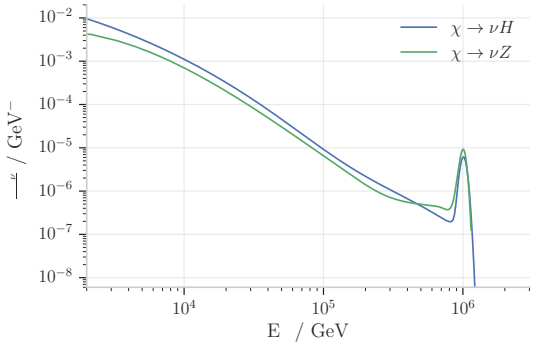


Figure 1: Benchmark neutrino spectra simulated from the kinematics and secondary processes (Spectra for the track-analysis from [13]). The simulated spectra are smeared out with a 5% log-normal distribution for numerical stability and shown here exemplary assuming a 2 PeV dark matter particle.

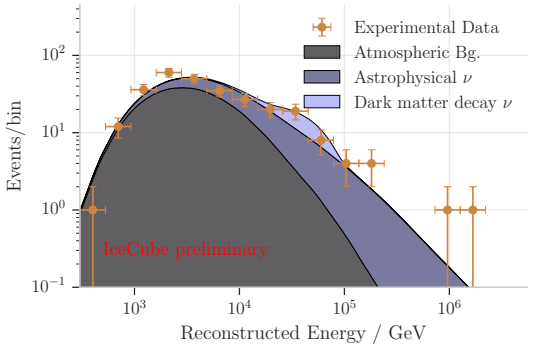


Figure 2: Cascade-Analysis: Best-fit energy distribution using the background plus dark matter decay signal hypothesis. The excess at ~30 TeV leads to the dark matter signal being fitted at a mass of 100 TeV, it is well compatible with a background fluctuation though.

best-fitting dark matter mass and lifetime are different in both analyses and the track analysis observes a larger significance (p = 3.5%). Figures 2 and 3 show the best-fit flux components together with the experimental data as a function of reconstructed energy.

While the significance of the result from the cascade-analysis is low ($p = 55\%$) and a strong contribution from dark matter can thus be excluded, further investigations are needed for the track-analysis. A real dark matter signal should exhibit a clear signature both in the energy distribution and the arrival directions, that is certain bins are expected to dominate the fit if a non-zero dark matter contribution is found. Figure 4 shows the significance per bin as a function of arrival directions revealing some differences between detector seasons; The events observed with the IC79 configuration indeed show a correlation between positive significance and the direction of the halo (similar but less strong observed in the seasons IC59 and IC86-1, not shown). The last three years of data (IC86-234), on the other hand, do not confirm this observation. A dark matter signal is expected to be constant in time and this anomaly may indicate a statistical fluctuation (Therefore, lower limits on the dark matter lifetime are computed in Sec. 5 for both analyses).

	Track sample		Cascade sample	
	Bg.	Signal+Bg.	Bg.	Signal+Bg.
m_{DM} / PeV	-	1.3	-	0.1
τ_{DM} / 10^{27}s	-	22	-	8.2
Astrophysical norm. / 10^{-18}GeV^{-1}cm^{-2}sr^{-1}s^{-1}	0.97	0.16	2.17	1.63
Astrophysical spectral index	2.16	1.99	2.72	2.78
$TS = 2 \times \Delta LLH$	$6.7 \to p = 0.035$		$3.4 \to p = 0.55$	

Table 2: Best-fit parameters for both analyses. The quoted p-values are obtained from background pseudo-experiments.

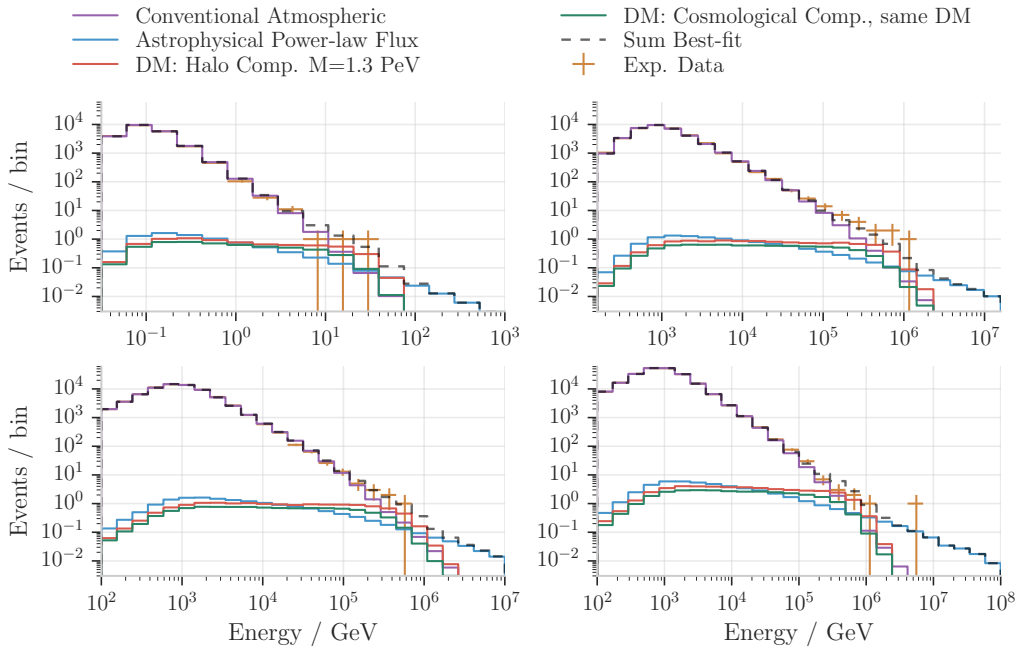


Figure 3: Track-Analysis: Best-fit energy distributions. While the low energetic events are well described by the conventional atmospheric component, the high energetic events are modelled by a combination of a weak diffuse flux and a component from decaying dark matter ($m_{DM} = 1.3\,\text{PeV}, \tau_{DM} = 2.2 \times 10^{28}\,\text{s}$). The four histograms of the different detector configurations are shown separately for technical reasons but the fit was performed simultaneously with all seasons.

4.1 Systematic Uncertainties

To study the systematic uncertainties arising from imperfect modelling of flux components, ice properties and the behaviour of the detector, dedicated simulation datasets are used. In the track-analysis, the impact of the following parameters is quantified and then parametrized as continuous nuisance parameters before the fit [2]: Normalization of the conventional and prompt atmospheric fluxes, cosmic-ray flux model uncertainties, relative contribution from Pion and Kaon decays to the atmospheric fluxes, several optical properties of the glacial ice and its modelling in the analysis and at last the optical efficiency of the detector modules. Their influence on the dark matter hypothesis turns out to be negligible because they are constrained by the low-energy region of the data with high statistics. In the cascade analysis, conventional and prompt atmospheric flux uncertainties [6], angular errors due to ice model uncertainties [14], 10% uncertainty on the DOM efficiency and the impact of the finite simulation statistics are taken into account. The green dashed limit shown in figure 5 shows the impact of these systematics (no corresponding line for track-analysis because the impact is negligible). The overall effect is 10%-15% for DM masses below 5 PeV and <1% above.

A strong systematic uncertainty is the modelling of the dark matter flux prediction in both analyses. While the ΛCDM-parameters used in the cosmological component were measured to reasonable precision ($\Delta\Omega/\Omega < 3\%$), large uncertainties have to be taken into account for the halo component: The parameters of the Burkert profile are varied within their stated error ellipse (pre-

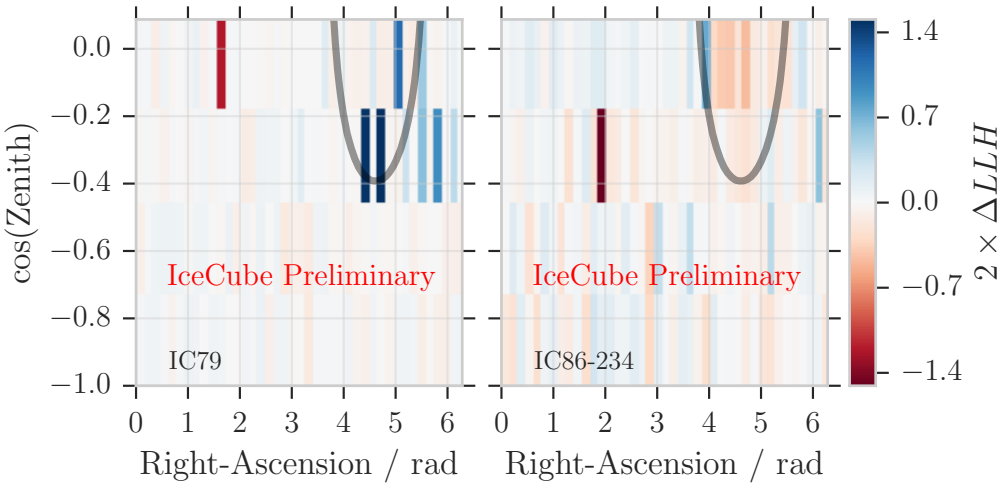


Figure 4: Track-Analysis: Significance per bin for the IC79 and IC86-234 configuration. Blue bins indicate where the signal hypothesis is preferred and vice versa. For comparison, the direction of the halo (half peak density) is shown as grey band.

ferred best-fit for $\beta_2 = -0.5$, see discussion in [11]) and the maximal impact on the dark matter flux is evaluated (shaded bands around the limit curves in figure 5). This leads to a systematic uncertainty of approximately 10%. For the track-analysis, it gives simultaneously an estimation of the uncertainty due to the choice of the Halo profile (NFW-profile prediction as second benchmark has smaller deviations.)

Last we note, that the tested hypothesis assumes a single power-law for the diffuse astrophysical flux. Deviations from the power-law assumption would have an effect on the results.

5. Lower Limits on the DM Lifetime

As a final result, limits on the lifetime of the dark matter particle are derived: Taking into account the observed differences between detector seasons, a (one-sided) lower limit relative to the background hypothesis is calculated as conservative approach in the track-analysis. The construction is based on Neyman confidence intervals [15], and relies on generated pseudo-experiments with dark matter signals injected. The resulting test-statistic distribution is compared to the experimental test-statistic value to calculate the limit contour at 90%CL (red line in figure 5).

For the cascade analysis, the Feldman-Cousins approach [16] is taken to construct the acceptance intervals. Dark matter lifetimes, for which the observed test statistic is incompatible with the acceptance intervals, are excluded. As no significant signal has been observed, a lower limit on the lifetime is obtained (90%CL, green line in figure 5). Figure 5 shows the limit contours from both analyses, also comparing to results from the IC22 and Fermi-LAT collaboration [17, 18].

In conclusion, two independent data samples containing 6 years of up-going tracks and 2 years of full-sky cascade events have been analysed. Although the fits in both analyses converge to a finite dark matter lifetime, they are consistent with background fluctuations. Excluded regions of the parameter-space are the currently best IceCube limit on the dark matter lifetime for dark matter masses above 10 TeV.

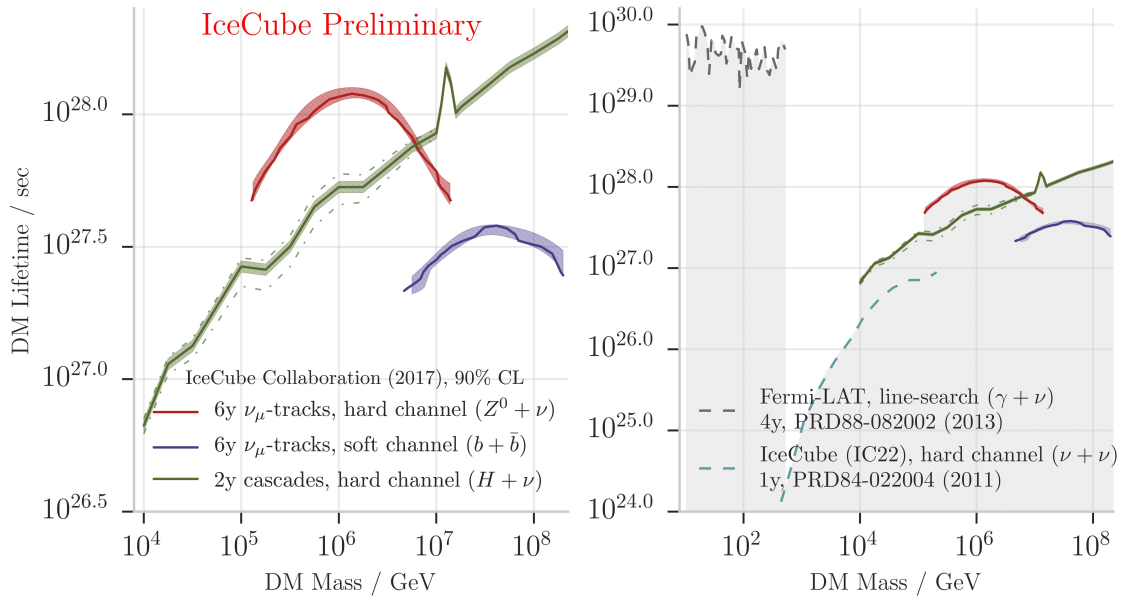


Figure 5: Lower limits on the dark matter lifetime as a function of the dark matter mass. Left: Results from this paper including systematics; For the track-analysis, additionally a converted limit assuming a soft decay channel ($b+\bar{b}$) is presented. The influence of detector systematics is negligible in the track-analysis (no dashed line). Right: Comparison to results from the Fermi and IceCube (IC22) collaborations.

References

[1] **IceCube** collaboration, M. G. Aartsen et al., *Physical Review Letters* **113** (2014) 101101.

[2] **IceCube** collaboration, M. G. Aartsen et al., *The Astrophysical Journal* **833** (2016) 3.

[3] **IceCube** collaboration, M. G. Aartsen et al., *The Astrophysical Journal* **835** (2017) 151.

[4] L. Covi et al., *Journal of Cosmology and Astroparticle Physics* (2010) .

[5] **IceCube** collaboration, *Journal of Instrumentation* **12** (2017) P03012.

[6] **IceCube** collaboration, M. G. Aartsen et al., *Physical Review D* **91** (2015) 022001.

[7] M. Honda et al., *Physical Review D* **75** (2007) 043006.

[8] Enberg, R. and others, *Physical Review D* **78** (2008) 043005.

[9] F. Halzen, *Journal of Physics: Conference Series* **337** (2012) 012050.

[10] A. Esmaili et al., *Journal of Cosmology and Astroparticle Physics* **1412** (2014) 054.

[11] F. Nesti and P. Salucci, *Journal of Cosmology and Astroparticle Physics* **1307** (2013) 016.

[12] **Planck** collaboration, P. A. R. Ade et al., *Astronomy and Astrophysics* **594** (2016) A13.

[13] J. Pepper, Ph.D. thesis, The University of Alabama, 2017.

[14] **IceCube** collaboration, M. G. Aartsen et al., arXiv:1705.02383.

[15] J. Neyman, *Philosophical Transactions of the Royal Society of London. Series A, Mathematical and Physical Sciences* **236** (1937) 333–380.

[16] G. J. Feldman and R. D. Cousins, *Physical Review D* **57** (1998) 3873–3889.

[17] **IceCube** collaboration, R. Abbasi et al., *Physical Review D* **84** (2011) 022004.

[18] **Fermi-LAT** collaboration, M. Ackermann et al., *Physical Review D* **88** (2013) 082002.

PROCEEDINGS OF SCIENCE

Latest results and sensitivities for solar dark matter searches with IceCube

The IceCube Collaboration[†]

[†] *http://icecube.wisc.edu/collaboration/authors/icrc17_icecube*

E-mail: seongjin.in@gmail.com

Dark matter from the Galactic dark matter halo could scatter off of nuclei in the Sun and become gravitationally captured, accumulating in the center. The accumulated dark matter may annihilate into standard model particles and produce energetic neutrinos in sequent decays. Neutrinos with energies below a few hundred GeV escape the Sun without any significant absorption and can be searched for using a neutrino telescope. IceCube has produced the most stringent bounds on spin-dependent scattering of dark matter with hydrogen by looking for this signal. We present IceCube's latest solar dark matter search results including a new all-neutrino flavor result that substantially improves IceCube's sensitivity for dark matter particles with masses below O(100) GeV.

Corresponding authors: Seongjin In[1]* **and Klaus Wiebe**[2]

[1]*Department of Physics, Sungkyunkwan University, Seobu 16419, Suwon, South Korea*

[2]*Johannes Gutenberg University Mainz, Germany*

35th International Cosmic Ray Conference ICRC2017
10-20 July, 2017
Bexco, Busan, Korea

*Speaker.

PoS(ICRC2017)912

1. Introduction

Dark matter (DM) annihilations in the Sun could result in observable signals at neutrino telescopes. IceCube, the worlds largest neutrino observatory [1], located in South Pole, has searched for such signals from the Sun and we present a status of on-going searches as well as an outlook for future analyses and detector upgrades.

Dark matter (denoted χ) from the Galactic dark matter halo can be gravitationally captured by to the Sun after an initial scattering of Hydrogen or heavier nuclei. Dark matter will accumulate in the center of the Sun and is expected to self-annihilate in many popular DM scenarios, such as Weakly Interactive Massive Particles (WIMPs). Under the assumption that DM capture and annihilation have reached equilibrium, the expected neutrino flux is independent of the dark matter self-annihilation cross section and only depends on the scattering process that initiates capture. The equilibrium assumption [2] is reasonable given the age of the Sun and allows for an easy conversion of a neutrino flux to a corresponding WIMP-proton cross section. The expected neutrino energy range of interest for IceCube is from few GeV to 1 TeV, as neutrino signals above 100 GeV start to be attenuated due to absorption in the Sun.

In these proceedings we summarize results using muon neutrinos and three years of IceCube data [3]. We present a new all-flavor search for solar WIMPs [4] and give an outlook in future solar WIMP searches with IceCube and planned upgrades.

2. Solar Dark Matter annihilation search with 3 years of IceCube data

Solar Dark Matter annihilation search with IceCube-79strings (IC79) was performed in 2011 and we have updated this analysis with 3 years data with the final 86-string detector configuration (IC86). The sensitivity is better than the previous due to the additional statistics and improved analysis method. As a low energy point-like source analysis, the angular resolution of the detector is important. Therefore, ν_μ samples are the main focus of this analysis.

For the signal simulation, we used DarkSUSY [5] and WimpSim [6] to calculate the predicted neutrino signal flux and the propagation to the Earth, taking neutrino oscillations into account.

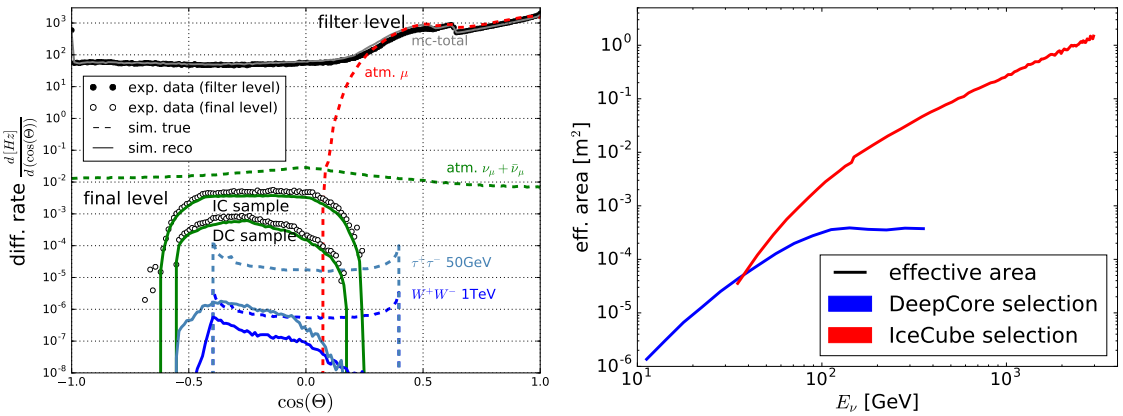


Figure 1: Right: simulation and data comparison as function of the cosine of zenith angle. Left: effective area as function of the reconstructed energy.

PoS(ICRC2017)912

Backgrounds of this analysis are atmospheric neutrinos and muons. The CORSIKA package [7] is used to calculate the interaction of comic rays with the Earths atmosphere for the atmospheric μ background. For the atmospheric ν background, we used neutrino-generator (NuGen) and GENIE respective for energies above and below 150 GeV.

2.1 Event selection and Analysis

We define two events selections optimized to different neutrino energy ranges. The first one referred to as DeepCore (DC), selects events that interact in the DeepCore detector, while the second sample, classified as IceCube (IC), sample focuses on more energetic neutrino events. To point events back to the Sun we optimize for muon neutrinos. We only select upgoing events and utilize the Earth as a filter against atmospheric muons μ, this analysis mainly is focused on the upgoing events that starts below the detector and travel upwards through it. IC sample was optimized for neutrino events with energies above $\sim$100 GeV.

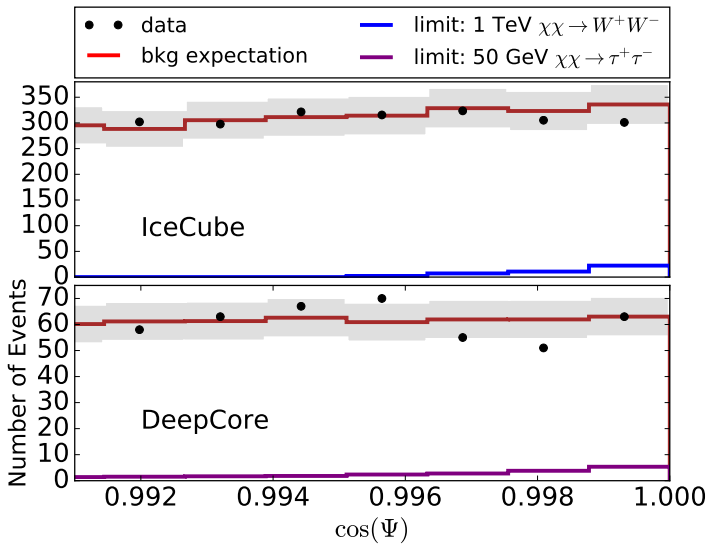


Figure 2: Events distribution for cosine of angular distance from the Sun. Black dots show the reconstructed data at the corresponding direction. The red lines are background expectation from MC simulation and gray regions represent statistical uncertainties on the background expectation. Blue ($\chi\chi \to W^+W^-$) and purple($\chi\chi \to \tau^+\tau^-$) lines are the expected solar WIMPs annihilation events in IceCube and DeepCore, respectively.

Figure 1 shows differential rates backgrounds at filter and final selection cut level for IC and DC samples. The background predictions are compared to observed event rates and signal expectations at current bounds. The points represent the data and lines show the simulation expectations. Dotted lines show the simulation prediction before the event selection. The red dotted line represents simulated atmospheric μ and green dotted line shows simulated atmospheric ν_μ. Downgoing events are dominated by atmospheric μ as without the Earth veto effect. The light blue and dark blue lines are the predicted neutrino flux from solar WIMP annihilations in the Sun respective for $\chi\chi \to \tau^+\tau^-$ and $\chi\chi \to W^+W^-$. After the event selection, we get green solid lines for the simulation and white dots as data. In the right of figure 1 the effective area for the IC and DC event selections are shown.

Figure 2 shows the distribution of neutrino events with respect to the cosine angular separation of the Sun for IceCube (top) and DeepCore (bottom) samples. We estimate WIMP-proton cross section limits with an unbinned maximum likelihood method. For N events with n_s signal events, the likelihood function is:

PoS(ICRC2017)912

$$L(n_S) = \prod_N \left(\frac{n_s}{N} S_i + \left(1 - \frac{n_s}{N}\right) B_i\right) \tag{2.1}$$

S_i and B_i are probability density functions(p.d.f.) for signal and background respectively and depend on the reconstructed energy and position of the events. Each p.d.f. can be written as

$$S_i(\vec{x}_i, t_i, E_i; m_\chi, c_\chi) = K(|\vec{x}_i - \vec{x_\odot}|, k_i) \times \varepsilon_{m_\chi, c_\chi}(E_i) \tag{2.2}$$

$$B_i(\vec{x}_i, E_i) = D(\delta_i) \times P(E_i|\phi_{atm}) \tag{2.3}$$

The energy part of signal p.d.f. is dependent on the WIMPs mass (m_χ) and capture coefficient (c_χ). K represents the angular distribution of the signal with the concentration factor, k_i and is given by the Fisher-Binghan distribution [8]. The background p.d.f. consists of the declination dependence (D) and the distribution (P) of the energy estimator, E in the event sample.

2.2 Results

There is no significant excess of events in the direction of the Sun. Assuming a local DM density of 0.3GeV/cm^3, a standard Maxwellian halo velocity distribution and the Standard Solar Model, we calculate the upper limit of the spin-dependent WIMP-proton cross section in IceCube (figure 3). We include 12-35% systematic uncertainties dependent on the WIMPs masses. IceCube limits are the most stringent above ∼80 GeV (thick solid lines). Our limit excludes the models from a scan of ∼500 million points in the 19 parameters of the phenomelogical minimally super-symmetic standard model (pMSSM) calculated by micrOMEGAs [9].

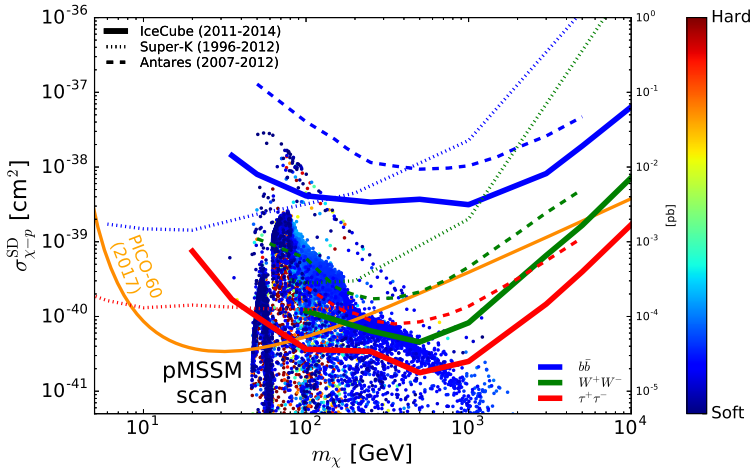


Figure 3: WIMP-proton spin dependent cross section with 3 years data of IceCube. Each color represents a different annihilation channel; blue - $b\bar{b}$, green - W^+W^-, red - $\tau^+\tau^-$. As the reference limits, we marked Super-K (dotted) and Antares (dashed) limit and from the direct detection PICO-60 C_3F_8 (orange) [10].

3. All-flavor search for solar WIMPS

The denser low energy infill, DeepCore, considerably improves neutrino detection with energies below 100 GeV due to the higher sensor granularity and the veto capacity of the surrounding IceCube strings. IceCube can detect all flavors of active neutrinos through Cherenkov light emission from secondary particles created when a neutrino interacts in the ice. The reconstruction of electron and tau neutrino interactions, leaving cascade-like signatures in the detector, is more challenging than the reconstruction of track-like signatures. However, all-neutrino searches have

PoS(ICRC2017)912

become in focus recently. The reasons are obvious [11]: the measured flux is enhanced, the neutrino energies may be determined to a better precision, backgrounds from atmospheric ν_e and ν_τ are smaller and cosmic ray muons tend to be rejected better by requiring that the events have a cascade-like signature.

3.1 Analysis

An exploratory study of IceCube's sensitivity to WIMP annihilations in the center of the Sun with an analysis that is sensitive to all flavors of neutrinos was performed on data taken with the finalized configuration in the 2011 season. For the simulation of a WIMP-induced neutrino signal, the *WimpSim* package [6] was used which takes care of neutrino generation, propagation and oscillations.

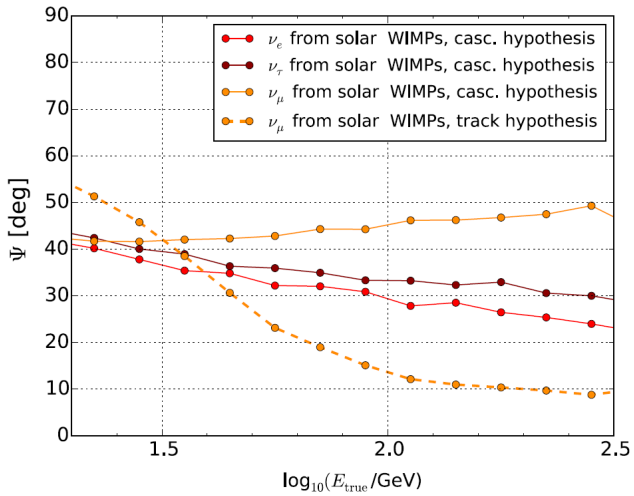


Figure 4: Median angular distance between simulated and reconstructed direction at the final selection level. Solid lines correspond to a cascade reconstruction while the dashed line represent a reconstruction assuming a track hypothesis.

Unlike the extended tracks caused by muons from charged-current (CC) ν_μ events, ν_e and ν_τ leave an almost spherical pattern of hit DOMs in the detector. The $e^\pm$ produced in CC ν_e interactions are subject to successive bremsstrahlung energy losses and lead to electromagnetic cascades. ν_τ interactions and τ decays predominantly produce hadronic cascades, as do neutral current interactions from all neutrino flavors. While the energy reconstruction benefits from the confined event signature, a good directional reconstruction of the spherically shaped cascade events demands significant computing resources and also an excellent description of the ice properties. Energy E, position and orientation are estimated [12] by minimizing the negative log-likelihood $-\ln L = \sum_i k_i \ln(E\Lambda_i + \rho_i) - (E\Lambda_i - \rho_i) - \ln k_i!$, where ρ_i is the expected number of noise photons and k_i is the observed number of photons in a time bin i.

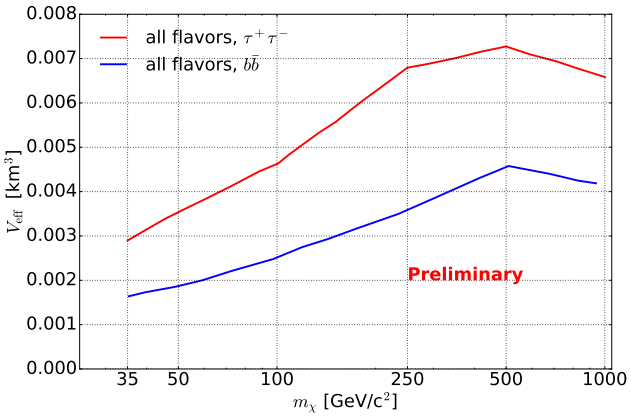


Figure 5: Final level effective volume as function of WIMP mass for soft ($b\bar{b}$) and hard annihilation ($\tau^+\tau^-$) channels.

The number of photons per unit energy for an assumed orientation and vertex Λ_i incorporates detailed information on the position dependent absorption and scattering of photons in the ice. This information is available in the form of spline-fitted tables obtained from a photon-tracking simulation using a ray tracing algorithm modeling scattering and absorption. When iterating the minimization chain (in this analysis 32 times) and optimizing minimiza-

PoS(ICRC2017)912

tion parameters, the resulting angular resolutions are similar to the ones seeded by the true direction and vertex.

The energy dependent median spatial angle resolution is shown in Fig. 4. Since no reliable flavor identification is possible on an event by event basis without substantial efficiency losses, the cascade hypothesis is used for all events. It is evident from Fig. 4 that the cascade reconstruction is actually superior to the track hypothesis reconstruction for all all neutrino species with energies below 35 GeV.

Individual event resolutions may vary from the average resolution dependent on the event's exact topology and the amount of light deposited in the detector volume. Since event-based resolutions allow for a reconstruction quality based event weighting, a resolution estimator, based on the Cramer-Rao upper bound on the variance, was coded [4].

In a series of selection levels, the dominant background from atmospheric muons is reduced, followed by filters that effectively remove noise clusters and coincidences,

	$b\bar{b}$			$\tau^+\tau^-$			W^+W^-		
m_χ [GeV/c^2]	ε [%]	$\mu_{\text{fit}}^{90\%}$ [events]	$\sigma_{\text{SD}}^{\chi,p}$ [fb]	ε [%]	$\mu_{\text{fit}}^{90\%}$ [events]	$\sigma_{\text{SD}}^{\chi,p}$ [fb]	ε [%]	$\mu_{\text{fit}}^{90\%}$ [events]	$\sigma_{\text{SD}}^{\chi,p}$ [fb]
35	12.0	157	1.8	10.2	145	0.1	-	-	-
50	10.6	141	2.0	8.1	137	0.1	-	-	-
100	7.9	139	2.7	4.3	103	0.1	4.7	106	0.22
250	4.5	119	5.0	2.3	72	0.14	2.2	69	0.34
500	3.3	113	10	1.6	54	0.29	1.5	47	0.72
1000	2.0	77	23	1.2	40	0.75	1.1	39	2.6

Table 1: Selected final level efficiencies (ε) with respect to level 2, best fit sensitivity on number of signal events and spin-dependent WIMP cross section limits, $\sigma_{\text{SD}}^{\chi,p}$ (excluding systematic uncertainties).

Finally, a set of Boosted Decision Trees (BDTs) using 12 variables, including reconstructed direction, energy and vertex, reconstruction quality parameters as well as veto and geometrical quantities, was trained to discriminate signal-like from background-like events [4]. The BDT score cut was optimized to provide the best sensitivity for a given WIMP mass and annihilation channel. Signal efficiencies (ε) for WIMPs with masses below 250 GeV/c^2 are listed in Table 1.

For the distinction of signal and background events, a likelihood code [13] commonly employed in IceCube point source searches was adapted. The code, which includes event-based energy and angular uncertainty information, was altered substantially to work for cascade-shaped events with large angular uncertainties. For example, the signal PDF was expressed analytically by a von Mises-Fisher distribution and the background and energy PDFs were represented by a spline-smoothed two-dimensional histogram, where the binning was optimized automatically for each BDT score.

3.2 Systematic uncertainties

The likelihood analysis uses scrambled experimental data for the background level estimation, which therefore is not subject to atmospheric flux models, neutrino cross sections and the detector modeling. The sensitivities and upper limits, however, are calculated by injecting simulated signal

PoS(ICRC2017)912

events and as such depend on the correct modeling of the detector response and particle physics uncertainties, such as oscillation parameters and neutrino cross section in the transition region to deep inelastic scattering. Astrophysical uncertainties, like the local dark matter density and local velocity, are also important.

The dominant detector related uncertainty, especially at low energies, is the absolute DOM light detection efficiency of roughly 10%. Its effect on the signal was assessed by the productin of datasets with artificially lowered and increased efficiencies, leading to asymmetric uncertainty estimates. The total uncertainty, including effects from the ice model, neutrino cross sections and oscillations,ranges between 16.6% and 21%, slightly depending on the annihilation channel and assume WIMP mass. For this study a local dark matter density of $\rho_0 = 0.30\ \mathrm{GeV}/c^2/\mathrm{cm}^3$ was adapted. The results can be easily rescaled as the limits scale inversely with the assumed matter density (larger densities yield sensitivities to smaller WIMP scattering cross sections).

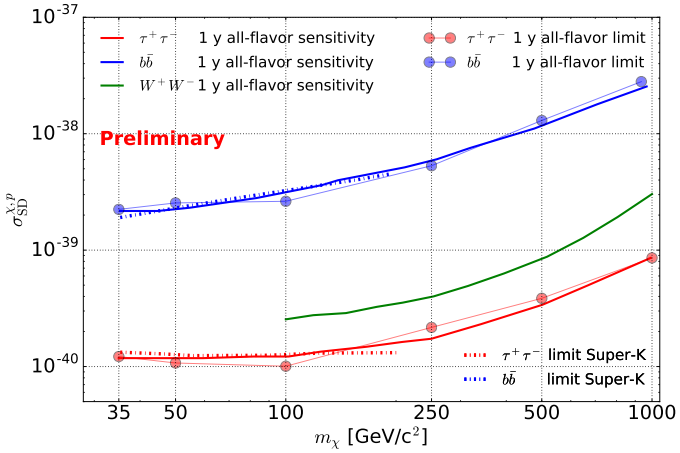


Figure 6: Upper limits and sensitivities for the $b\bar{b}$ and $\tau^+\tau^-$ channels.

4. Solar WIMP sensitivity for IceCube-Gen2/PINGU

IceCube-Gen2/PINGU is a proposed extension of IceCube envisioned to include the deployment of 20 densely instrumented strings in the central region of IceCube. IceCube-Gen2/PINGU is expected to significantly improve the sensitivity for WIMP masses in the energy range between 5 and 50 GeV. Building on the experience gained with DeepCore analyses we perform a straight-

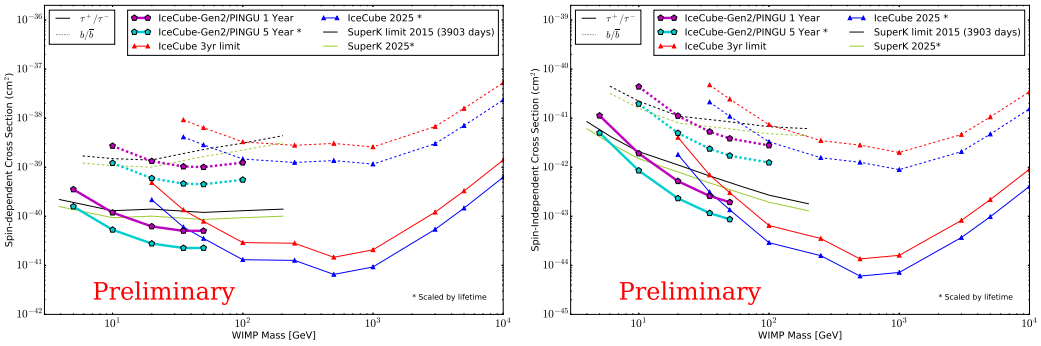


Figure 7: Sensitivity of the 26×192 IceCube-Gen2/PINGU baseline geometry to $\sigma_{p,SD}$ (left figure) and $\sigma_{p,SI}$ (right figure) for hard (solid lines) and soft (dashed lines) annihilation channels over a range of WIMP masses for livetimes of one (magenta) and five (green) years. The sensitivities are compared to the present IceCube limits [3] and limits from Super-K [14], as well as limits projected to the year 2025 to compare to the IceCube-Gen2/PINGU sensitivities.

PoS(ICRC2017)912

forward event-based Monte Carlo (MC) study, using the 26×192 IceCube-Gen2/PINGU baseline geometry. We use standard event selection criteria and apply a fixed search window around the position of the Sun with a half-cone opening angle of 10°. Figure 7 shows the sensitivity for IceCube-Gen2/PINGU combined with the scaled currently best published IceCube limit.

5. Summary and Outlook

IceCube has searched for dark matter captured in the Sun and produced some of the most stringent limits on the spin-dependent WIMP-nucleon scattering cross section. A new analysis using all neutrino flavors has significantly improved sensitivities for WIMP masses below 50 GeV. While high-energy neutrinos (> 1 TeV) cannot escape the center of the Sun due to absorption, energetic neutrinos could be produced in scenarios with secluded dark matter. In such a scenario DM annihilates into long lived mediators which can escape from the Sun, and could decay into neutrinos [15, 16]. Cosmic-ray interactions in the solar atmosphere could also produce energetic neutrinos and are lately of high theoretical interest [17] [18]. Solar atmospheric neutrinos pose a natural background to solar dark matter searches. Analyses efforts in IceCube have started to target energetic neutrinos from the Sun [19]. Lastly with the Gen2 extension to the IceCube detector the sensitivity to dark matter masses below 100 GeV can be significantly improved.

References

[1] **IceCube** Collaboration, M.G. Aartsen *et al.*, *JINST* **12** (2017) P0301.

[2] G. Jungman, M. Kamionkowski, K. Griest, *Phys. Rept.* **267** (1996) 195.

[3] **IceCube** Collaboration, M.G. Aartsen *et al.*, *Eur. Phys. J.* **C77** (2017) 146

[4] **IceCube** Collaboration, Klaus Wiebe and Anna Steuer, PoS(ICRC2015)1224 (2015).

[5] P. Gondolo, J. Edsjö, P. Ullio, L. Bergström,M. Schelke and E.A. Baltz, *JCAP* **07** (2004) 008.

[6] M. Blennow, J. Edsjö and T. Ohlsson, *JCAP* **01** (2008) 021.

[7] D. Heck *et al.*, (Forschungszentrum Karlsruhe) Tech. Rep. FZKA-6019 (1998).

[8] J.T. Kent, J. Royal. *Stat. Soc.* **44** (1982) 71.

[9] G. Belanger *et al.*, *Comput. Phys. Commun.* **185** (2014) 960.

[10] **PICO** Collaboration, C.Amole *et al.*, *Phys. Rev. Lett* **118** (2017) 251301.

[11] C. Rott, T. Tanaka and Y. Itow, *JCAP* **1109** (2011) 029.

[12] **IceCube** Collaboration, M. G. Aartsen *et al.*, *JINST* **9** (2014) P03009.

[13] **IceCube** Collaboration, Stephan Coenders PoS(ICRC2015)1047 (2015).

[14] **Super-Kamiokande** Collaboration, K. Choi *et al.*, *Phys. Rev. Lett.* **114** (2015) 141301.

[15] N. F. Bell and K. Petraki, *JCAP* **1104** (2011) 003.

[16] P. Meade, S. Nussinov, M. Papucci and T. Volansky, *JHEP* **1006** (2010) 029.

[17] C.A. Argüelles, G. de Wasseige, A. Fedynitch and B.J.P. Jones, [astro-ph/1703.07798].

[18] Kenny C. Y. Ng, John F. Beacom, Annika H. G. Peter and C. Rott, [astro-ph/1703.10280].

[19] **IceCube** Collaboration, Seongjin In and Carsten Rott PoS(ICRC2017)965 (these proceedings).

PoS(ICRC2017)912

PROCEEDINGS OF SCIENCE

Searches for annihilating dark matter in the Milky Way halo with IceCube

The IceCube Collaboration[†]

[†] *http://icecube.wisc.edu/collaboration/authors/icrc17_icecube*

E-mail: samuel.d.flis@gmail.com

We present three searches for a neutrino signal from dark matter self-annihilations in the Milky Way. The signal from these events is identified by signatures which start developing within the fiducial volume of the IceCube Neutrino Observatory. The three presented analyses are sensitive to different energy scales and together cover an energy range from 10 GeV to 300 TeV in dark matter particle mass, while focusing on either track-like or cascade-like events. Two analyses incorporate energy in the analysis, while one analysis introduces a novel method to reconstruct events below 1 TeV. Experimental exclusion limits are presented for all analyses.

Corresponding authors: Samuel Flis[*1], Morten Medici[2]

[1] *Oskar Klein Centre and Dept. of Physics, Stockholm University, SE-10691 Stockholm, Sweden*

[2] *Niels Bohr Institute, University of Copenhagen, DK-2100 Copenhagen, Denmark*

35th International Cosmic Ray Conference — ICRC2017
10–20 July, 2017
Bexco, Busan, Korea

[*] Speaker.

PoS(ICRC2017)906

1. Introduction

So far dark matter has only revealed its presence by its gravitational influence. Measurements of galactic rotation curves [1, 2] and movements of galaxies in clusters such as the Coma cluster [3] indicate a much larger mass than could be accounted for by only observing the luminous matter. Currently our best description of the Universe is given by the ΛCDM [4] model in which cold non-baryonic dark matter is a crucial ingredient. The nature of dark matter is still unknown, however it has to be fairly long lived given the current observational and experimental constraints, and it may interact weakly.

Many theories that extend the Standard Model predict particles with properties which fit the above description of dark matter. One of the most experimentally accessible dark matter candidates are the so-called Weakly Interacting Massive Particles (WIMPs) [5]. If these particles self-annihilate they might produce stable Standard Model particles, such as electrons, photons or neutrinos that are detectable at Earth. It is compelling to search for a neutrino signal from dark matter annihilation since neutrinos, which only interact weakly, propagate through the Universe largely unaffected. The direction and energy information that can be extracted from neutrinos will be unchanged from their creation even considering neutrino vacuum oscillations.

The rate of self-annihilation increases with the dark matter density making regions with presumably higher dark matter densities such as massive celestial objects, galaxies and dwarf galaxies interesting from an observational point of view. Galaxies are believed to be embedded in halos of dark matter that extend far beyond the optical disks of the galaxies. The differential neutrino flux from annihilating dark matter in the Milky Way assuming a dark matter particle mass, m, a neutrino energy spectrum from annihilating dark matter $\mathrm{d}N/\mathrm{d}E$ and a thermally averaged cross-section $\langle\sigma v\rangle$ is given by

$$\frac{\mathrm{d}\Phi}{\mathrm{d}E} = \frac{\langle\sigma_A v\rangle}{4\pi \cdot 2m^2}\frac{\mathrm{d}N}{\mathrm{d}E}\int \rho^2(r(l,\Psi))\mathrm{d}l, \tag{1.1}$$

where $\rho(r)$ is the dark matter density profile and the integral is evaluated along the line of sight. A variety of models try to describe the distribution of dark matter in galactic halos where spherical symmetry is often assumed. N-body simulations have commonly favored cuspy density profiles like the NFW profile which tend to diverge towards the center [6], while observations of low surface brightness galaxies suggest a flat (also called cored) distribution in the central region which in this work has been represented by the Burkert halo profile [7]. Figure 1 illustrates the two dark matter density profiles and how the line of sight integral, $J(\Psi)$, depends on the angle to the Galactic Center. Since it is still not clear whether the Milky Way halo is cuspy or cored we present results for both of the two halo profiles, using model parameter values from Ref. [8].

Three analyses are presented here, probing WIMP masses from 10 GeV to 300 TeV using neutrino data from the IceCube Neutrino Observatory[9]. IceCube instruments one cubic-kilometer of glacier ice at the geographical South Pole using 5160 detectors distributed on 86 strings. Neutrinos are detected by the Cherenkov radiation produced by secondary charged leptons created in neutrino interactions in the ice. Different event topologies (corresponding to different neutrino interactions) are used in the three analyses. Track-like events induced by muon neutrinos have good directional reconstruction in general, and are used in the first two analyses presented. The third

PoS(ICRC2017)906

analysis uses shower (cascade) events induced by charge-current interactions of electron and tau neutrinos as well as neutral current interactions from all neutrino flavors. Cascade events provide a better energy reconstruction at the price of poor pointing accuracy.

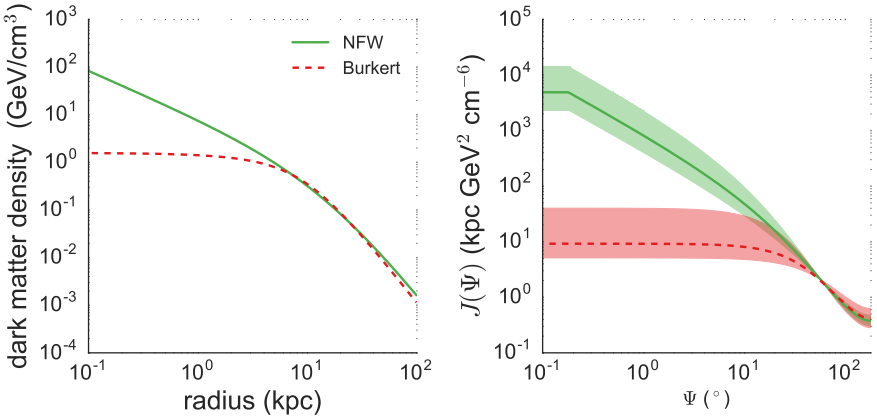


Figure 1: Left: Dark matter density profiles as a function of the distance to the center of the galaxy. **Right:** The line of sight integral for different profiles as a function of the angle to the center of the galaxy.

2. Analysis method

The analyses presented here use the same likelihood approach to search for a neutrino excess aligned with the Galactic Center that corresponds with dark matter annihilation in the Milky Way halo. The likelihood is defined as a mixture of signal, S, and background, B, and can generally be written down as

$$\mathscr{L}(\xi) = \prod_i \left[\xi S(\theta_i) + (1-\xi)B(\theta_i)\right] \tag{2.1}$$

where ξ is the signal fraction and θ_i are the event observables. Signal is modeled by weighting simulated neutrino events with Eq. 1.1. The neutrino energy spectrum is determined from `PYTHIA8` [10] simulation by forcing a generic resonance of twice the dark matter mass to decay into one of the considered dark matter annihilation channels. The background is estimated from experimental data, so will not be affected by systematic uncertainties from the simulation chain. However, due to the extended nature of the Milky Way halo, if a signal is present, the background estimation will be contaminated with signal. If the signal contamination is not accounted for it leads to biased estimators and a reduction of the analysis sensitivity. We counter the signal contamination by applying a signal subtraction method. The scrambled data is modeled as $\tilde{D} = \xi\tilde{S} + (1-\xi)B$ where the tilde denotes a scrambled quantity. Solving this for B and putting it back into Eq. 2.1 yields the final form of the likelihood:

$$\mathscr{L}(\xi) = \prod_i \left[\xi S(\theta_i) + \tilde{D}(\theta_i) - \xi\tilde{S}(\theta_i)\right]. \tag{2.2}$$

PoS(ICRC2017)906

3. Low-Energy Galactic Center tracks

A muon produced in a muon neutrino chargedcurrent interaction can travel many hundred meters through the ice. This allows for a good reconstruction of the neutrino direction, since it is well correlated to that of the muon. The dark matter analyses that are focused on muon track events are exploiting the pointing precision of the track to look for an anisotropy corresponding to the targeted signal from dark matter annihilation.

Below neutrino energies of 100 GeV, the muon tracks are more challenging to reconstruct, and are no longer clearly distinguishable from cascade events. However, with the improvement of IceCube event reconstruction, it has been possible to improve the sensitivity of IceCube to neutrino energies below 100 GeV. These improvements therefore make it possible for the low energy analyses to be sensitive to WIMP masses down to 10 GeV.

The event sample used in the low energy analysis is specifically designed for WIMP masses between 10 GeV and 1 TeV, with details explained in Ref. [11]. The IceCube/DeepCore sub-detector is used as the fiducial volume for the analysis, using the strings indicated in Figure 2, with detectors located between a depth of 2140-2420 m.

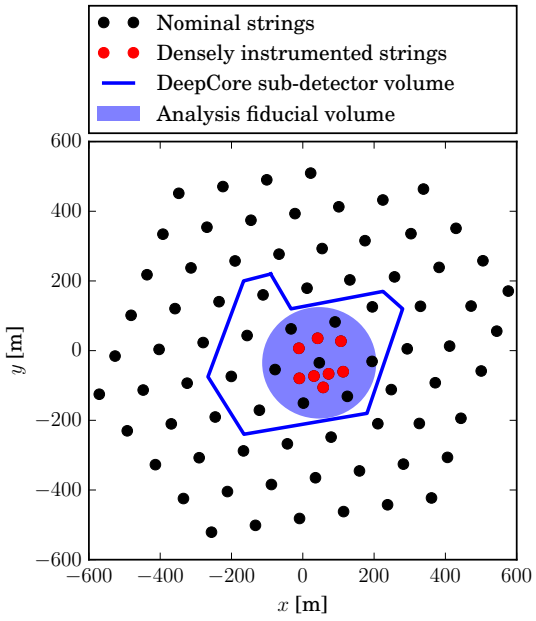


Figure 2: Fiducial volume of the sub-detector IceCube/DeepCore and the volume used for the analysis of the low energy galactic center search.

The remainder of the IceCube strings are used to tag and reject the massive background of down-going atmospheric muons. Muon neutrinos with a reconstructed arrival direction close to the center of the Milky Way in declination are primarily selected, however, interacting electron neutrinos and tau neutrinos (as well as neutral-current interactions) are also included.

In the analysis of the experimental data, all events are included if they have a reconstructed arrival direction in the full band of right ascension across the sky at a declination interval 2 radi-

PoS(ICRC2017)906

ans wide (centered on the galactic center). Since the atmospheric background is uniform in right ascension, most of the sensitivity of the analysis comes from studying this dimension.

The data were collected between 2012 and 2015 using the full 86-string configuration of IceCube with the sample containing 22 632 events in total. In Figure 3 the declination bin covering the galactic center is presented, and the different expectations from the two dark matter halo models considered. Additionally this shows that no strong signal above the constant background was observed in data.

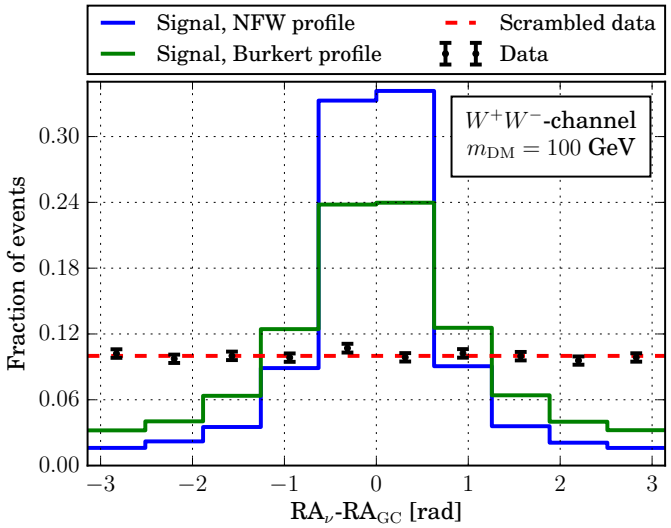


Figure 3: Distribution of events in right ascension for the low energy galactic center search, showing no excess above the flat background expected from atmospheric muons and neutrinos.

4. High-Energy Galactic Halo tracks

At higher energies the signal efficiency of muon neutrino induced through-going events grows faster than the efficiency to detect starting events. This analysis therefore used event samples with through-going events that traditionally were used for Point Source (PS) searches in IceCube [12, 13, 14]. Four years of IceCube data were used, spanning from the 40-string configuration of IceCube to the 86-string configuration. The PS datasets cover the full sky, however the atmospheric muon background is poorly suppressed in the southern hemisphere (the down-going region) compared to the northern hemisphere where the atmospheric muons are absorbed by Earth.

A dedicated point source neutrino sample for the southern hemisphere named Medium Energy Starting Events (MESE) [15] was also added. This sample consists of three years of data and the veto cut ensures a low muon background for the MESE sample. Even with the addition of the MESE sample an analysis on the combined sample is mostly sensitive in the northern hemisphere, and thus primarily probes the outer halo. An advantage of mainly probing the outer halo is the smaller dependence on the halo profiles which tend to converge at larger distances to the Galactic center.

PoS(ICRC2017)906

The analysis of the PS and MESE data samples was performed using an unbinned likelihood including both directional and energy observables. As the data samples were collected and processed under varying conditions, the background and signal was modelled specifically for each sample. In the end the likelihoods for each sample were combined into a joint likelihood.

5. High-Energy Galactic Halo cascades

This search uses starting events that are cascade-like, i.e. resembling electromagnetic or hadronic showers, presumably induced by neutrino interactions in the ice. Cascade events have the advantages of better energy reconstruction (due to the containment of the complete energy loss) and all-flavor sensitivity. The directional reconstruction is of course much worse compared to tracks, however, in the context of resolving the Milky Way halo which extends over the whole sky and in particular the Galactic Center region which covers several degrees, the effect of the reduced resolution of cascade events is mitigated. In contrast to the first IceCube dark matter search that used cascades [16], this search is focusing on relatively high WIMP masses.

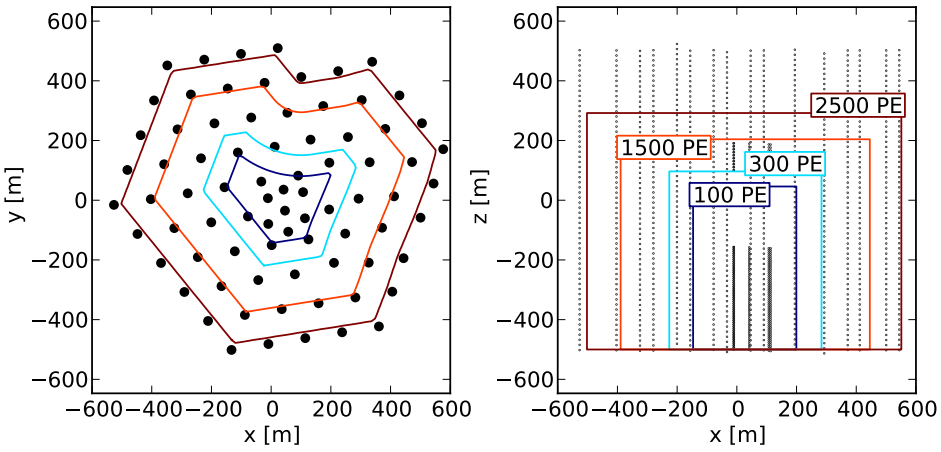


Figure 4: An illustration of how the fiducial volume grows with the detected deposited charge in a top down perspective (left) and a side view (right)

The event sample used in this analysis was originally developed for an unfolding analysis of different components of the neutrino spectrum observed at Earth [17]. The data were collected between 2010 and 2012 using one year of the 79-string configuration and the first year of the full 86-string configuration of IceCube. The events in the sample are required to start inside a fiducial volume which scales with the detected deposited charge of the event. Figure 4 illustrates how the fiducial volume scales for different amounts of deposited charge. The remaining volume serves as a veto region to reject incoming muons as well as distinguish between cascade events and outgoing track events. This analysis only considered events that were classified as cascades. In total the two samples contained 278 cascade events where 133 events were collected with the 79-string detector and 145 events were collected with the 86-string detector.

PoS(ICRC2017)906

The data from the two years had separate geometries, calibrations, and separate simulation datasets, hence the two samples were treated separately. A binned likelihood analysis using energy and directional observables was performed. Similar to the previously described halo track analysis the likelihoods for the two samples were combined into a joint likelihood.

6. Results and conclusions

None of the analyses observed any excesses above the expectation from the background of atmospheric muons and atmospheric neutrinos, and instead limits on $\langle \sigma_A v \rangle$ were set. All analyses computed limits at 90% confidence according to Feldman and Cousins prescription [18]. Figure 5 shows the resulting limits assuming dark matter annihilation into tauons and an NFW profile (left panel) or a Burkert profile (right panel). Besides limits from the analyses presented here, limits from ANTARES and gamma ray telescopes are shown. Both the gamma ray experiments and the ANTARES analysis set limits that are lower than the IceCube limits for most of the mass range when assuming the NFW profile. However, when considering the Burkert profile, IceCube sets the most stringent limits along most of the mass range. IceCube analyses probe the full sky or at least a large portion of the sky and are therefore less sensitive to variations between profiles in the central region of the Galactic Center. Probing a large part of the sky is also advantageous in the case of extended profiles such as the cored Burkert halo where 90% of the signal is contained within $10^\circ - 15^\circ$ in the sky. This is best illustrated with the high-energy galactic halo track search (IC 4yr PS) that essentially only probes the outer halo and produces very similar limits for both profiles.

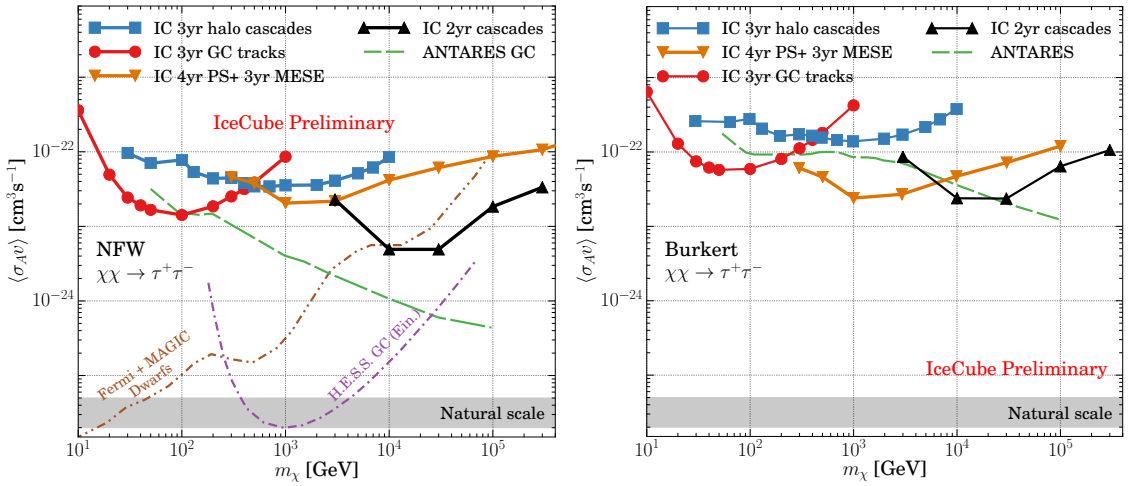


Figure 5: Comparison of upper limits on $\langle \sigma_A v \rangle$ versus WIMP mass, for the annihilation channel $\chi\chi \to \tau^+\tau^-$, assuming the NFW profile (left) and the Burkert profile (right). The analyses presnted here are compared to ANTARES [19] and the IceCube 3yr halo search [16]. Also shown are upper limits from gamma-ray searches from the dwarf galaxy Segue 1 (Seg1) by FermiLAT+MAGIC [20] and the Galactic Center by H.E.S.S. [21]. The natural scale refer to the value of $\langle \sigma v \rangle$ that is needed for WIMPs to be a thermal relic [22]

PoS(ICRC2017)906

References

[1] H. W. Babcock, Lick Observatory Bulletin **19** (1939) 41

[2] V. C. Rubin and Jr. W. K. Ford, Astrophys. J. **159** (1970) 379

[3] F. Zwicky, Helvetica Physica Acta **6** (1933) 110

[4] **Planck** Collaboration, P. A. R. Ade et al., Astron. Astrophys. **594**, A13 (2016)

[5] J. E. Gunn, B. W. Lee, I. Lerche, D. N. Schramm and G. Steigman, Astrophys. J. **223** (1978) 1015

[6] J. F. Navarro, C. S. Frenk and S. D. M. White, Astrophys. J. **462** (1996) 563

[7] A. Burkert, Astrophys. J. **447** (1995) L25

[8] F. Nesti and P. Salucci, JCAP **1307** (2013) 016

[9] **IceCube** Collaboration, M. G. Aartsen et al., JINST **12** (2017), P03012

[10] T. Sjostrand, S. Mrenna and P. Z. Skands, Comput. Phys. Commun. **178** (2008) 852

[11] **IceCube** Collaboration, M. G. Aartsen et al., arXiv:1705.08103 [hep-ex].

[12] **IceCube** Collaboration, R. Abbasi et al., Astrophys. J. **732** (2011) 18

[13] **IceCube** Collaboration, M. G. Aartsen et al. Astrophys. J. **779** (2013) 132

[14] **IceCube** Collaboration, M. G. Aartsen et al. Astrophys. J. **796** (2014) 109

[15] **IceCube** Collaboration, M. G. Aartsen et al., Astrophys. J. **824** (2016) L28

[16] **IceCube** Collaboration, M. G. Aartsen et al., Eur. Phys. J. C **76** (2016) 531

[17] **IceCube** Collaboration, M. G. Aartsen et al., Phys. Rev. D **91** (2015) 022001

[18] G. J. Feldman and R. D. Cousins, Phys. Rev. D **57** (1998) 3873

[19] A. Albert et al., Phys. Lett. B **769** (2017) 249

[20] **MAGIC** and **Fermi-LAT** Collaborations, M. L. Ahnen et al., JCAP **1602** (2016) 039

[21] **H.E.S.S.** Collaboration, H. Abdallah et at., Phys. Rev. Lett. **117** (2016) 111301

[22] G. Steigman, B. Dasgupta, and J. F. Beacom, Phys. Rev. D **86** (2012) 023506

PoS(ICRC2017)906

PROCEEDINGS OF SCIENCE

Searches for Dark Matter in the center of the Earth with the IceCube detector

The IceCube Collaboration[†]
[†]*http://icecube.wisc.edu/collaboration/authors/icrc17_icecube*
E-mail: jan.lunemann@vub.ac.be

Several models predict that dark matter is constituted of Weakly Interacting Massive Particles (WIMPs). Such particles would be attracted by the gravity of massive astronomical objects such as black holes, stars, and the Earth. WIMPs can lose energy through scattering with matter and become trapped in the gravitational field of these objects. They can then annihilate or decay resulting in production of Standard Model particles. The neutrinos thus created will escape, as they pass through ordinary matter almost unaffected. This contribution describes the search for WIMPs accumulated in the center of the Earth using the IceCube neutrino observatory located at the geographic South Pole. Results from the analysis with one year of IceCube data from 2011 will be presented along with the sensitivity for several additional years of data.

Corresponding authors:I. Ansseau[1], J. Lünemann[*2],J. Aguilar[1]
[1] *Université Libre de Bruxelles*
[2] *Vrije Universiteit Brussel*

35th International Cosmic Ray Conference - ICRC2017
10-20 July, 2017
Bexco, Busan, Korea

[*]Speaker.

PoS(ICRC2017)896

1. Introduction

In 1933, Fritz Zwicky obtained evidence of unseen mass that he called *dunkle Materie*, 'Dark Matter' [2], in the Coma cluster of galaxies. More than 80 years after the discovery of missing mass, the physical origin of dark matter is still unclear. Several candidates have been proposed[3], the most discussed of which is the weakly interacting massive particle (WIMP). Heavy celestial bodies, such as the Earth, can potentially capture WIMPs. The accumulated WIMPs can then self-annihilate at a rate proportional to their number density in the Earth, thus generating neutrinos with a spectrum that depends on the WIMP mass and annihilation channel.

2. The IceCube Neutrino telescope

IceCube is a cubic-kilometer neutrino detector installed in the ice at the geographic South Pole [4] between depths of 1450 m and 2450 m, completed in 2010. Reconstruction of the direction, energy, and flavor of the neutrinos relies on the optical detection of Cherenkov radiation emitted by charged particles produced in the interactions of neutrinos in the surrounding ice or the nearby bedrock. The DeepCore subarray as defined in this analysis includes 8 densely instrumented strings optimized for low energies plus 12 adjacent standard strings.

While the large ice overburden above the detector provides a shield against downward going, cosmic ray induced muons with energies $\lesssim$ 500 GeV at the surface, most analyses focus on upward going neutrinos employing the entire Earth as a filter. Additionally, low energy analyses use DeepCore as the fiducial volume and the surrounding IceCube strings as an active veto to reduce penetrating muon backgrounds. The search for WIMP annihilation signatures at the center of the Earth takes advantage of these two background rejection techniques as the expected signal will be vertically up-going and of low energy.

3. Earth Dark Matter searches with IceCube

To estimate a flux of neutrino coming from the annihilation of WIMPs in the center of the Earth, we have to know the cross section for scattering by nuclei in the Earth, the capture rate C , the annihilation rate Γ_a and the probability to have a production of a neutrino through the decay of their annihilation products. The theoretical framework used to calculate the first two can be found [26]. If this capture rate C is constant, the WIMP annihilation Γ_a is given by : $\Gamma_a = \frac{C}{2}\tanh^2(\sqrt{CC_A}t)$. With C_A the probability of WIMP pair annihilation per unit time.

Γ_a has to be evaluated at $t_\oplus = 4.5x\ 10^9$years, the present age of the Earth. But $\sqrt{CC_A}t_\oplus$ is smaller than 1. The equilibrium has not yet been reached, and so the annihilation rate is not maximum.

C, the WIMP capture rate, depends on their mass, their velocity in the halo, and their local density. The velocity distribution is assumed to be Maxwellian ('Standard Halo Model') with a dispersion of 270km/s. The value of the local Dark Matter density is still under debate [6], with estimates ranging from ≈ 0.2 GeV/cm^3 to ≈ 0.5 GeV/cm^3.

We adopt a value of 0.3 GeV/cm^3 as suggested in [7] in order to compare to other such studies. If the WIMP mass is nearly identical to that of one of the nuclear species in the Earth, the capture rate will increase considerably, as shown in Fig. 1.

PoS(ICRC2017)896

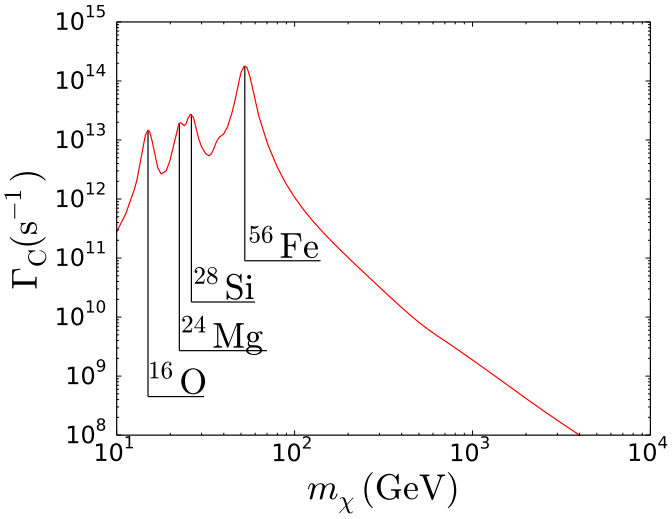


Figure 1: Rate at which WIMPs particles are captured in the interior of the Earth [8] for a scattering cross section of $\sigma_{SI} = 10^{-44}$ cm^2 . The peaks correspond to resonant capture on the most abundant elements in the Earth [9]: ^{56}Fe, ^{16}O, ^{28}Si and ^{24}Mg and their isotopes.

The capture rate could be higher if the velocity distribution of WIMPs with respect to the Earth is skewed towards low values, as only WIMPs moving slower than the Earth's escape velocity of 30km/s can be captured.

4. Background

As signal neutrinos originate near the center of the Earth, they induce a vertically up-going signal in the detector. This is however a special direction in the geometry of IceCube, as the strings are also vertical. While in other point source searches, a signal-free control region of the same detector acceptance can be defined by changing the azimuth, this is not possible for an Earth WIMP analysis. Consequently, a reliable background estimate can only be derived from simulation.

Two types of background have to be taken into account: the first type consists of atmospheric muons produced by cosmic rays in the atmosphere above the detector. Although these particles enter the detector from above, a small fraction will be reconstructed incorrectly as up-going.

The second type of background consists of atmospheric neutrinos. This irreducible background is coming from all directions.

5. Analysis : One year

The one-year analysis used the data taken in the first year of the fully deployed detector (from May 2011 to May 2012) with a livetime of 327 days. During the optimization of the event selection, only 10% of the complete dataset was used to check the agreement with the simulations. The size of this dataset is small enough to not reveal any potential signal, and hence allows us to maintain statistical blindness.

PoS(ICRC2017)896

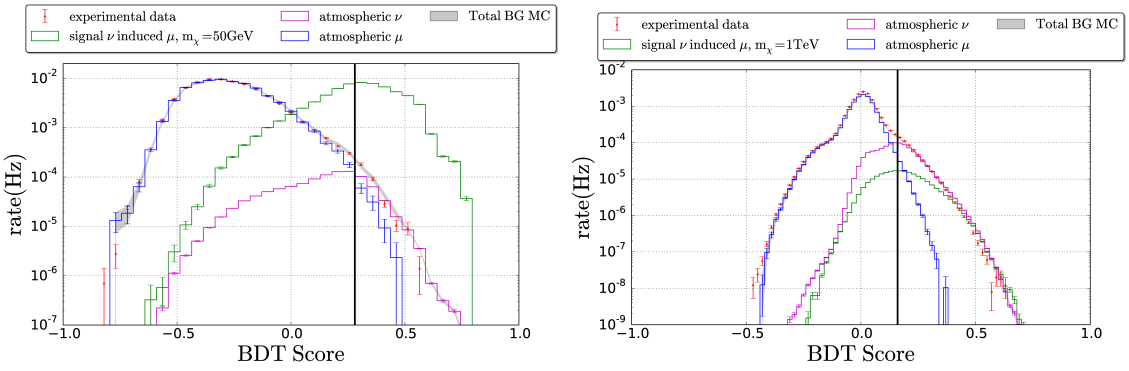


Figure 2: BDT score distributions at pre-BDT level for the low energy analysis (left) and for the high energy analysis using the *Pull-Validation* method (right). Signal distributions are upscaled to be visible in the plot. Signal and backgrounds are compared to experimental data from 10% of the first year of IC86 data. For the atmospheric neutrinos, all flavors are taken into account. In gray, the sum of all simulated background is shown. The vertical lines indicate the final cut value used in each analysis, where high scores to the right of the line are retained.

To be sensitive to a wide range of WIMP masses, the one year analysis is split into two parts that are optimized separately. The high energy event selection aims for an optimal sensitivity for WIMP masses of 1 TeV and the $\chi\chi \rightarrow W^+W^-$ channel. The event selection for the low energy part is optimized for 50 GeV WIMPs annihilating into tau leptons.

After a first set of linear cuts, the datasample is split regarding reconstructed energy. Both analyses use Boosted Decision Trees (BDTs) to classify background and signal events. This machine learning technique is designed to optimally separate signal from background after an analysis-specific training [10] by assigning a score between -1 (background-like) and +1 (signal-like) to each event.

Due to small statistics of simulation we found it necessary to apply the smoothing techniques described bellow. The high energy analysis uses *Pull-Validation* [11], a method to improve the usage of limited statistics.

The low energy analysis tackles the problem of poor statistics of the atmospheric muon background simulation in a different way. In this part of the analysis, only a single BDT is trained (Fig. 2-left), and after the cut on the BDT score, the reconstructed zenith distribution is smoothed using a Kernel Density Estimator (KDE) [12, 13] with gaussian kernel and choosing an optimal bandwidth [14].

To analyze the dataset for an additional neutrino signal coming from the center of the Earth, we define a likelihood test, that has been used in several IceCube analyses before (e.g. [15, 16]). Based on the background (f_{bg}) and signal distribution (f_s) of space angles Ψ between the reconstructed muon track and the Earth center (i.e. the reconstructed zenith angle), the probability to observe a value Ψ for a single event is $f(\Psi|\mu) = \frac{\mu}{n_{obs}} f_s(\Psi) + (1 - \frac{\mu}{n_{obs}}) f_{bg}(\Psi)$. Here, μ specifies the number of signal events in a set of n_{obs} observed events. The likelihood to observe a certain number of events at specific space angles Ψ_i is defined as $\mathscr{L} = \prod_i^{n_{obs}} f(\Psi_i|\mu)$. Following the procedure in [17], the ranking parameter $\mathscr{R}(\mu) = \frac{\mathscr{L}(\mu)}{\mathscr{L}(\hat{\mu})}$ is used as test statistic for the hypothesis testing, where $\hat{\mu}$ is the best fit of μ to the observation. A critical ranking $\mathscr{R}^{90}$ is defined for each signal strength, so

PoS(ICRC2017)896

that 90% of all experiments have a ranking larger than $\mathscr{R}^{90}$. This is determined by 10^4 pseudo experiments for each injected signal strength. The sensitivity is defined as the expectation value for the upper limit in case that no signal is present. This is determined by generating 10^4 pseudo experiments with no signal injected.

Due to the lack of a control region, the background estimation has to be derived from simulation. Therefore, systematic uncertainties of the simulated datasets were carefully studied. The effects of the uncertainties were quantified by varying the respective input parameters in the simulations.

Different types of detector related uncertainties have to be considered : the efficiency of the DOM to detect Cherenkov photons, the anisotropic scattering in the South Pole ice, the reduced scattering lenght of photons in the refrozen ice of the holes, the scattering and absorption lenghts. The uncertainties on the models of the background physics are also taken into account : the atmospheric flux, the neutrino oscillation parameters, the neutrino-nucleon cross section, the rate of coincidences of atmospheric neutrinos and atmospheric muons. Adding these uncertainties in quadrature results in a total of +34%/-48% in the low energy analysis and +32%/-35% for high energies. For the limit calculation, they are taken into account by using a semi-bayesian extension to the Feldman-Cousins approach [18].

6. Result : One year

As mentioned before, only 10% of the data were used for quality checks during the optimization of the analysis chain. Half of this subsample was used to train the BDTs and therefore these events could not be used for the later analysis. After the selection criteria were completely finalized, the zenith distributions of the remaining 95% of the dataset were examined (Fig. 3). No statistically significant excess above the expected atmospheric background was found from the direction of the center of the Earth.

Using the method described in Section 5, upper limits at the 90% confidence level on the volumetric flux $\Gamma_{\mu\to\nu} = \frac{\mu_s}{t_{\text{live}}\cdot V_{\text{eff}}}$ were calculated from the high and the low energy sample for WIMP masses between 10 GeV and 10 TeV in the hard and in the soft channel. The 90% C.L. limits obtained are shown in Fig. 4. The upper limit on the number of signal neutrinos, the volumetric flux, the WIMP annihilation rate inside the Earth and the resulting muon flux can be found in the paper [1].

7. Outlook : analysis multi-years

IceCube is currently in the process of a preparing a multi-year analysis. Using more than one year of data will improve the sensitivity by a factor of the square root of the number of years. In addition, a plan to improve the event selection is in the works. One such improvement would be to utilise IceCube hexagonal structure to reconstruct the track of the event. This analysis will also benefit from an improvement in reconstructions over previous analyses. The analysis will also focus more on the low energy region, where resonant capture will give stronger limits. We still have to make a positive identification of any Dark Matter particle, instead of only setting upper limits on their existence. The WIMP exclusion limits can move by varying the assumptions about their

PoS(ICRC2017)896

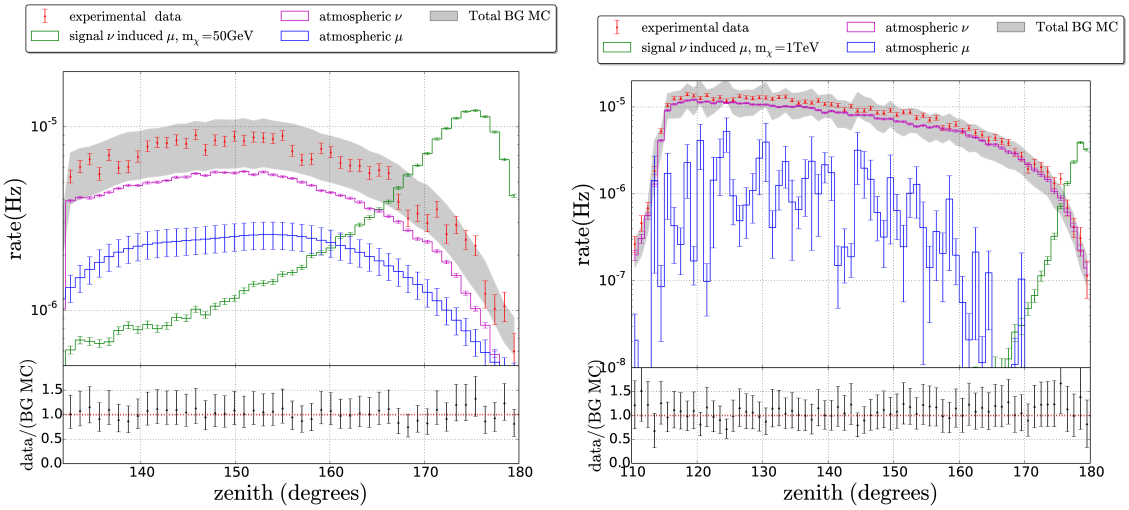


Figure 3: Reconstructed zenith distributions of 1 year of IC86 data (statistical uncertainties only) compared to the simulated background distributions, which include statistical and systematic uncertainties. For the atmospheric neutrinos, all flavors are taken into account. In the low energy analysis (left) the distributions were smoothed by a KDE and in the high energy analysis (right) the Pull-Validation method was used. Signal distributions are upscaled to be visible in the plot. The gray areas indicate the total predicted background distributions with 1 sigma uncertainties, including statistical and systematic uncertainties.

properties such as their speed, or the Galilean invariant interaction operators that can arise form the exchange of a heavy particle of spin less than or equal to one when WIMPs have spin 0, 1/2, 1[26]. So looking for WIMPs annihilations in the center of the Earth with the IceCube detector is still an important test. The sensitivity presented here will set strong limits on the existence of WIMPs.

8. Conclusion

Using one year of data taken by the fully completed detector, we performed the first IceCube search for neutrinos produced by WIMP dark matter annihilations in the center of the Earth. No evidence for a signal was found and 90% C.L. upper limits were set on the annihilation rate and the resulting muon flux as function of the WIMP mass. Assuming the natural scale for the velocity averaged annihilation cross section, upper limits on the spin-independent WIMP-nucleon scattering cross section could be derived. The limits on the annihilation rate are up to a factor 10 more restrictive than previous limits. For indirect WIMP searches through neutrinos, this analysis is highly complementary to Solar searches. In particular, at WIMP masses around 50 GeV, due to resonant capture by iron nuclei in the Earth the sensitivity of this analysis exceeds that of searches for WIMP annihilations in the Sun. The corresponding limit on the spin-independent cross section presented here is the best set presently by IceCube. The next analysis combining several years of data will further improve the sensitivity.

References

[1] **IceCube** Collaboration, M. G. Aartsen et al., *Eur. Phys. J. C* **77**, 82 (2017).

PoS(ICRC2017)896

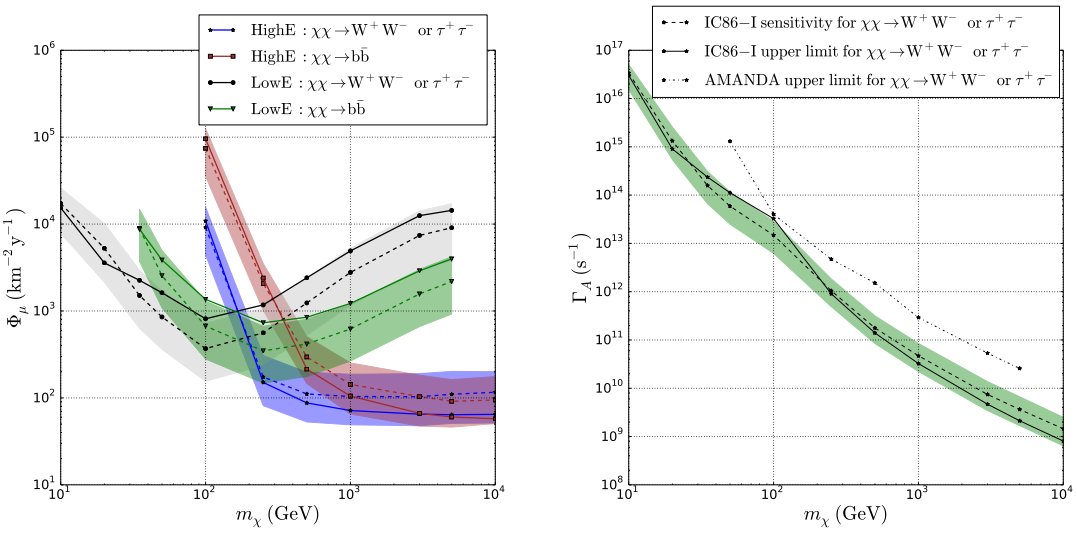


Figure 4: Right: Individual upper limits at 90% confidence level (solid lines) on the muon flux Φ_μ for the low and high energy analysis. Systematic uncertainties are included. For the soft channel, $\chi\chi \to b\bar{b}$ is assumed with 100% braching ratio, while for the hard channel the annihilation $\chi\chi \to \tau^+\tau^-$ for masses $\leq$ 50 GeV and $\chi\chi \to W^+W^-$ for higher masses is assumed. A flux with mixed branching ratios will be between these extremes. The dashed lines and the bands indicate the corresponding sensitivities with one sigma uncertainty. Left: The combined best upper limits (solid line) and sensitivities (dashed line) with 1 sigma uncertainty (green band) on the annihilation rate in the Earth Γ_A for 1 year of IC86 data as a function of the WIMP mass. For each WIMP mass, the sample (high energy or low energy) which yields the best sensitivity is used. Systematic uncertainties are included. The dotted line shows the latest upper limit on the annihilation rate, which was calculated with AMANDA data [19, 20].

[2] F. Zwicky *Helvetica Physica Acta* **6**, 110-127 (1933).

[3] G. Bertone et al., *Phys.Rept.* **405**, 279-390 (2005).

[4] **IceCube** Collaboration, M. G. Aartsen et al., *JINST* **12** (2017), P03012

[5] T. Bruch et al., *Phys. Lett. B* **674**, 250 (2009).

[6] J. I. Read, *J. Phys. G***41** 063101 (2014).

[7] **Particle Data** Group, K.A. Olive et al., *Chin. Phys. C38*, 090001 (2014).

[8] S. Sivertsson and J. Edsjö, *Phys. Rev. D* **85**, 123514 (2012).

[9] W.F. McDonough and S. Sun, *Chem. Geol.* **120**, 223 (1995).

[10] A. Hoecker et al., *PoS A CAT* **040**, (2007).

[11] **IceCube** Collaboration, M. G. Aartsen et al., PoS(ICRC2015)1211 (2016).

[12] M. Rosenblatt, *Ann. Math. Statist.* **27**, 832 (1956).

[13] E. Parzen, *Ann. Math. Statist.* **33**, 1065 (1962).

[14] B. W. Silverman, *Density Estimation for Statistics and Data Analysis*. London:Chapman & Hall (1986).

[15] **IceCube** Collaboration, M. G. Aartsen et al., *Phys. Rev. Lett.* **110**, 131302 (2013).

PoS(ICRC2017)896

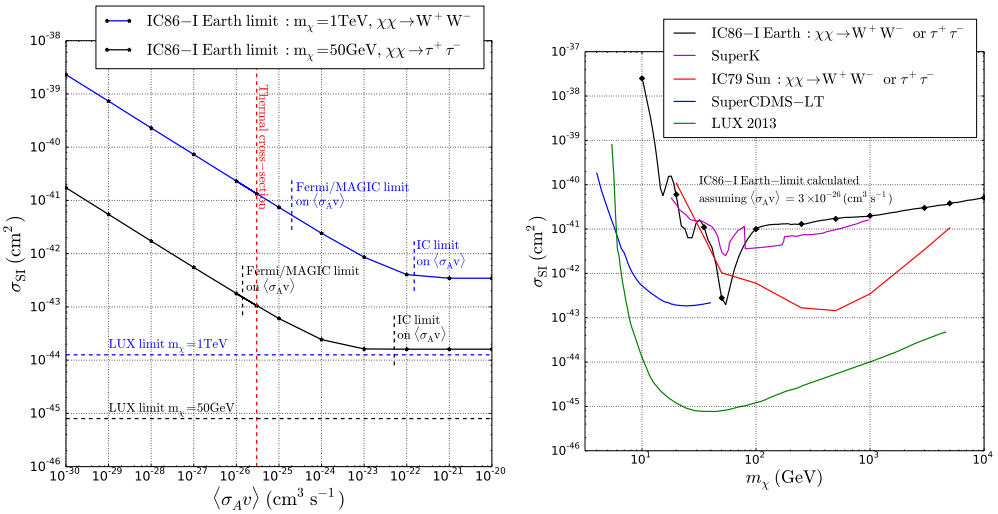


Figure 5: Right : Upper limits at 90% confidence level on $\sigma^{SI}_{\chi-N}$ as a function of the annihilation cross section for 50 GeV WIMPs annihilating into $\tau^+\tau^-$ and for 1 TeV WIMPs annihilating into W^+W^-. Systematic uncertainties are included. As a comparison, the limits of LUX [21] are shown as dashed lines. The red vertical line indicates the thermal annihilation cross section. Also indicated are IceCube limits on the annihilation cross section for the respective models [16], as well as the limits from a combined analysis of Fermi-LAT and MAGIC [22] Left : Upper limits at 90% confidence level on $\sigma^{SI}_{\chi-N}$ as a function of the WIMP-mass assuming a WIMP annihilation cross section of $\langle\sigma_A v\rangle = 3\cdot10^{-26}\mathrm{cm}^3\mathrm{s}^{-1}$. For WIMP masses above the rest mass of the W bosons, annihilation into W^+W^- is assumed and annihilation into $\tau^+\tau^-$ for lower masses. Systematic uncertainties are included. The result is compared to the limits set by SuperCDMSlite [23], LUX [21], Super-K [24] and by a Solar WIMP analysis of IceCube in the 79-string configuration [15]. The displayed limits are assuming a local dark matter density of $\rho_\chi = 0.3$ GeV cm^{-3}. A larger density, as suggested e.g. by [25], would scale all limits linearly.

[16] **IceCube** Collaboration, M. G. Aartsen et al., *Eur. Phys. J. C* **75**, 492 (2015).

[17] G. J. Feldman and R. D. Cousins, *Phys. Rev. D* **57**, 3873 (1998).

[18] J. Conrad, O. Botner, A. Hallgren, and C. Pérez de los Heros, *Phys. Rev.D* **67**, 012002 (2003).

[19] **AMANDA** Collaboration, A. Achterberg et al., *Astropart. Phys.* **26**, 129 (2006).

[20] A. Davour, PhD thesis, Universiteit Uppsala, (2007).

[21] **LUX** Collaboration, D. S. Akerib et al, *Phys. Rev. Lett.* **112**, 091303 (2013).

[22] M. L. Ahnen et al., *JCAP* **1602(02)**, 039 (2016).

[23] **SuperCDMS** Collaboration, R. Agnese et al., *Phys. Rev. Lett.* **112**, 041302 (2014).

[24] **Super-Kamiokande** Collaboration, S. Desai et al., *Phys. Rev. D* **70**, 083523 (2004).

[25] F. Nesti and P. Salucci, *J. Cosmology Astropart. Phys.* **1307**, 016 (2013).

[26] R. Catena [arXiv:astro-ph/1609.08967] (2017).

PoS(ICRC2017)896

PROCEEDINGS OF SCIENCE

Measurement of water luminescence - a new detection method for neutrino telescopes

The IceCube Collaboration[†]
[†] *http://icecube.wisc.edu/collaboration/authors/icrc17_icecube*
E-mail: anna.pollmann@uni-wuppertal.de

Large-scale neutrino telescopes use water or ice as a target medium. The detection of particles is therefore restricted to those which produce Cherenkov light, bremsstrahlung, or visible secondaries. This excludes the detection of slowly moving, massive particles proposed in theories which go beyond the standard model of particles, including magnetic monopoles.
Simulations show that these particles would be detectable with neutrino telescopes using a little known property of water: highly ionizing particles inducing the production of luminescence after passing through the water and exciting electronic states of the molecules or the lattice.
The few previous measurements of water luminescence show inconsistent results. In addition, there are no measurements with conditions comparable to those present in current large-scale neutrino telescopes. Measurements have therefore been designed that target these particular conditions and enable detailed investigations of the leading uncertainties.
Measurement results are presented and discussed in this contribution where the luminescence of water and ice is induced by α-particles. Measurements of warm ice $> -45\,^{\circ}\mathrm{C}$ are included which has never been considered before.

Corresponding authors: A. Pollmann*[1], S. Pieper[1]
[1] *Dept. of Physics, University of Wuppertal, 42119 Wuppertal, Germany*

35th International Cosmic Ray Conference – ICRC2017-
10-20 July, 2017
Bexco, Busan, Korea

*Speaker.

PoS(ICRC2017)1060

1. Luminescence of pure water and ice

Radio-luminescence is the excitation of transparent media by ionizing radiation resulting subsequently in visible light emission. In 1953 it was shown that pure ice itself emits luminescence light during irradiation [1]. The light was originally thought to originate from impurities in the ice.

Subsequently the effect was investigated in cold ice and liquid water. The measured luminescence yields G_α, that is the number of photons created per deposited α-energy E_α, $G_\alpha = dN_\gamma/dE_\alpha$ range from $0.2\,\gamma$/MeV to $20\,\gamma$/MeV (summarized in Fig. 5). Measurements of luminescence in warm ice ($> 220\,$K) are not published. The measured luminescence yields vary over orders of magnitude which may arise from different purification methods, saturation effects, or different time resolutions [2, 3]. Additionally the luminescence yield of cold ice is dependent on the temperature [4] and the variation of measurement results implies that it is also dependent on the irradiation type or charge due to quenching [5].

The emission spectrum of cold ice luminescence peaks at visible wavelengths with a dominant peak at about 390 nm [2, 3]. In addition to the spectrum, the half-lives of the excited states were used to identify the luminescence mechanisms. The measured half-lives range from af ew nanoseconds to several hundred nanoseconds in cold ice [3, 4]. It was deduced that the luminescence originates from certain transitions of excited OH^-, H_3O^+, H_2O, and solved O_2 molecules for different temperatures and emission wavelengths. The luminescence mechanisms in liquid water are yet to be identified.

In summary the characteristics of the luminescence of water and ice are not precisely known, especially not in the targeted temperature range from $-40\,^\circ$C to $+10\,^\circ$C.

2. Luminescence in neutrino telescopes

The largest neutrino detectors use water and ice as detection media in which charged particles with speeds exceeding $\sim 0.75\,c$ induce Cherenkov light emission. Luminescence enables observation of particles at lower speeds, thus it becomes a complementary method of particle detection.

At high energy detectors, such as IceCube, KM3NeT, and Baikal, luminescence enables the detection of slowly moving magnetically or highly electrically charged particles with unprecedented sensitivity [6]. These are particles that are proposed beyond the Standard Model of particle physics, one example are magnetic monopoles which have an equivalent charge of at least $68.5\,e$ [7].

Detectors for sub-GeV neutrinos, such as Super- and Hyper-Kamiokande, can detect slowly moving interaction products taking luminescence into account. An example is the kaons that could be produced via the proposed proton decay which, in this case, have an energy below the Cherenkov threshold in water [8].

Luminescence in neutrino detectors would, in addition, refine particle identification methods and the energy calibration of PeV-scale particles. The contribution of photons from luminescence can be up to 10% of the amount of Cherenkov photons when assuming an energy deposition in the PeV range.

At sub-GeV energies, particle identification is based on discrimination of sharp edged rings induced by muons on the one hand and blurred rings by electron induced cascades on the other

PoS(ICRC2017)1060

hand. Isotropic contributions, such as Rayleigh scattering and luminescence, hamper the discrimination power of reconstruction tools. The delayed emission of luminescence photons compared to Cherenkov photons adds to this reconstruction uncertainty. The particle identification could be improved if the features of luminescence could be included into simulation and reconstruction algorithms.

The contribution of salt water luminescence, as in the sea for KM3NeT or the salt phase of the Sudbury Neutrino Observatory and Super-Kamiokande-Gd, could be even larger [9, 10]. At detectors with artificial media, salt is added to enhance the neutron capture cross section and the delayed light signal. Identifying the coincidence of a positron with a delayed neutron capture significantly improves the sensitivity for Supernova events. However, the delayed neutron capture signal has to be discriminated from long decay times of luminescence.

Apart from one measurement by Baikal [11], there are no measurements covering the conditions of the large neutrino telescopes KM3NeT, ANTARES, IceCube, Super-Kamiokande(-Gd), Hyper-Kamiokande, or SNO and previous laboratory measurements vary significantly. Thus, luminescence of water and ice needs to be measured and characterized precisely for a future application at water and ice based particle detectors.

3. Measurement setup

A setup was developed to measure luminescence induced by α-particles emitted by an ^{241}Am source in ultra-purified water and ice, see Fig. 1. The light emission is recorded by a PMT. Measurements are performed inside a dark box which is placed in a freezer, that is used for temperature control.



Figure 1: Photograph of the setup for measuring the luminescence yield of ice (left) and water (right). The distance from PMT to sample surface was increased to take the picture.

For measurements above 0 °C, the ^{241}Am source is placed on a stainless steel cylinder inside the water sample that is stored in a sterile polypropylene cup. The single-use cup is manufactured for liquid biological samples of about 100 ml volume.

Bubble and crack free ice was grown by freezing purified and vacuum degassed water at $\approx -15\,^{\circ}$C within a sterile cup which was placed into a water-filled styrofoam box. The process was stopped after $\approx$ 12 hours when only $\approx$ 1 cm of ice was grown at the water surface. The lower ice

PoS(ICRC2017)1060

surface was straightened by placing it for ≈ 1 minute on a metallic surface at room temperature. The source was attached to the sterile upper ice surface which was then frozen at $\approx -20\,^{\circ}\mathrm{C}$ for 10 minutes. The ice was then placed upside-down on a cleaned aluminum foil to reflect photons upwards as shown in Fig. 2.

The purified water used in these measurements has a resistance of $> 18\,\mathrm{M\Omega cm}$ and total organic carbon (TOC) of $< 10\,\mathrm{ppb}$. All materials which have contact with the water, apart from the sterile cups, are cleaned by placing in purified water for at least several hours after conventional cleaning.

The source characteristics were measured with the same setup using a known scintillator and a ^{241}Am calibration source. The ^{241}Am source used has a surface emission rate of $(51 \pm 5)\,\mathrm{kBq}$ for α-particles over $2\pi\,\mathrm{sr}$. The emission energy of the 5.486 MeV α-particles was measured to be $(4.4 \pm 0.4)\,\mathrm{MeV}$ because the ^{241}Am is covered with a thin layer of gold by the manufacturer. α-particles of 4.4 MeV loose all energy within $\approx 11\,\mu\mathrm{m}$ in ice. X-rays are also produced from the source with highest intensities at 13.9 keV (37%) and 59.54 keV (35.9%) [12].

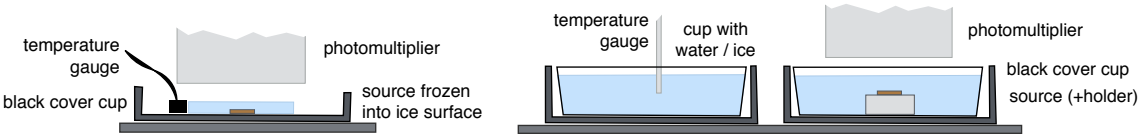


Figure 2: Schematic drawing of the setup for measuring the luminescence yield of ice (left) and water (right).

Photons, which might be created in the setup, are then detected by a photomultiplier tube (PMT) that was selected for single photon counting [13] and placed just above the water and ice surfaces over the source as shown in Fig. 1. In case of water this was done to avoid contaminations inside the purified water samples. The PMT was measured to be sensitive from 250 nm to 650 nm. It is operated with positive high voltage to avoid charge collection at the cathode. The efficiency of the PMT per wavelength was measured in comparison with a calibrated diode. It is maximal with $(27.2 \pm 1.3)\,\%$ at wavelengths of $(380 - 390)\,\mathrm{nm}$. It varies $\pm 1\%$ within an inner radius of 6 mm of the photo-cathode and drops afterwards approximatly linearly.

The non-amplified signal of the PMT is read out with a digital oscilloscope [14]. The peak value per triggered 100 ns sample is saved as the amplitude. The rate is calculated by dividing the number of triggered hits by the required recording time whereas the latter is obtained from the PC which drives the oscilloscope. The recording time was ensured to exceed 1 s to ensure small uncertainty on the measurement duration. The dead-time of the oscilloscope is lower than $1\,\mu\mathrm{s}$ and the reproduction of signal generator rates was checked up to 100 kHz. Other parameters are monitored to ensure stable conditions, i.e. room temperature, freezer temperature, environmental electromagnetic noise, PMT high voltage, CPU workload and room light.

4. Background

The contributions of different background sources, shown in Fig. 3, were measured to isolate the signal induced by α-particles in water, i.e. the PMT dark rate, environmental light, natural radioactivity, cosmic rays, X-rays from the source and electronic noise.

PoS(ICRC2017)1060

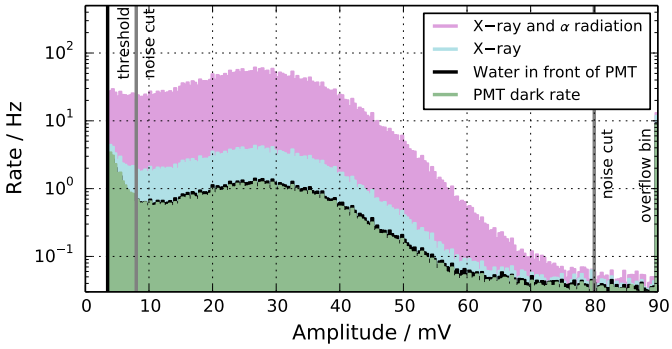


Figure 3: Background and signal contributions of luminescence induced with α-particles from ^{241}Am measured at 25 °C in ultra-purified water. The trigger threshold is at 4 mV. The last bin is an overflow bin. The main peak matches the position of the single photon peak. Noise was reduced by discarding events with peak amplitude below 8 mV and above 80 mV. The experimental procedure as well as the interpretation are explained in the text.

The measured PMT dark rate, shown in Fig. 3, includes negligible environmental light. A cup of water was placed in front of the PMT to measure the contribution of natural radioactivity in water, cup, and surroundings as well as cosmic ray interactions in the water.

The X-rays emitted by ^{241}Am undergo Compton scattering in media producing free low energetic electrons which produce luminescence. The light yield of Compton scattering in the PMT glass dominates over the light yield from scattering in water or other parts of the setup. The latter was determined by covering the PMT cathode with a black lid and placing the source beneath a black sheet of plastics in front of the PMT. The measured signal is well above the dark rate and shows a temperature dependence, see Sec. 5. The regarding light yield of glass scintillation is roughly $3\,\gamma$/MeV which is compatible with a previous glass scintillation measurement [15]. The Compton scattering in the cup or the ice holder was measured to be negligible. The summed contribution of X-rays, shown in Fig. 3, was measured by placing the source into the water (or below the ice) under a cover of black plastics. The contribution of α-irradiation of water over all background is then measured with the source in water (or frozen onto the lower surface of the ice) without any cover.

As shown in Fig. 3, the contribution of α-irradiation to the total light emission is significantly stronger than all background contributions which are subtracted in further calculations. For further analysis, all pulses with a peak amplitude between 8 mV and 80 mV, which translates to approximately $(0.25-2.5)$ PE, are kept to reduce electronic and environmental noise.

5. Temperature dependence

The temperature of the setup was adjusted using a freezer or by warming/cooling to/from room temperature outside the operational temperatures. The PMT base was covered with a thin plastic bag to prevent condensation on the electronics causing instable rates. The temperature of the water sample was estimated by measuring the temperature in the middle of a dummy sample which was treated identically to the irradiated sample and placed directly next to it. A temperature gauge was

PoS(ICRC2017)1060

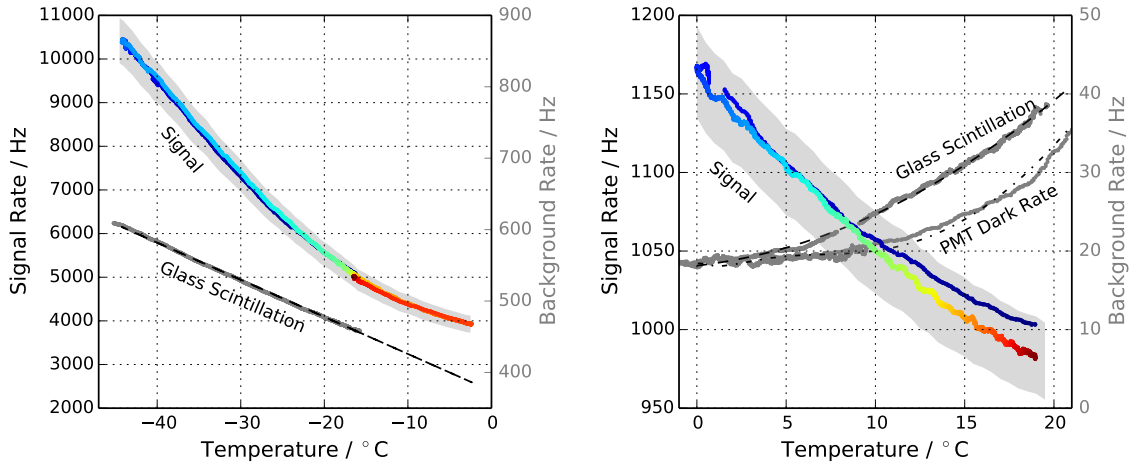


Figure 4: Temperature dependence of the light emission from α-irradiated ice (left) and water (right). The color scale shows the measurement time from blue over green and yellow to red. Gray bands indicate the measurement uncertainty of the rate. The temperature dependence of the setup, that is also shown, has been already subtracted from the signal shown here. The background rates are fit with a linear ($< 0\,^\circ$C) and polynomial ($> 0\,^\circ$C) distribution. Due to different geometries the absolute rates are not comparable.

frozen onto the side surface of the ice sample to measure its temperature. Data was taken during cooling and warming to ensure the absence of a significant hysteresis.

The temperature dependence of the PMT dark rate, the ice without source (to exclude tribo-luminescence), the water and ice under X-ray irradiation, and the glass scintillation was measured and subtracted from the rates shown in Fig. 4. A non-linear temperature dependence was measured which is slight for water and strong for ice irradiated by α-particles.

6. Discussion

A clear signal of single photons induced by α-irradiation of water and ice was isolated over background. This signal shows a temperature dependence in water and ice which is stronger than or inverted to all measured temperature dependencies of the setup. The Cherenkov threshold of $0.76\,c$ in ice is at $\approx 270\,\mathrm{keV}$ for electrons. α-particles with an energy of 5 MeV have a speed of $0.05\,c$ and the respective δ-electrons have a maximal energy of $\approx 3\,\mathrm{keV}$ [16]. Thus, no Cherenkov light is expected in this measurement. Additionally, Cherenkov light depends only on the speed of the incident particle and the medium's refractive index [17]. The latter is only slightly temperature dependent which does not explain the temperature dependence of the measured light.

The influence of solubles, originating from the materials in touch with the water samples, is tested by monitoring the signal rate directly after insertion of larger amounts of cleaned material into water for two days. No measurable effect was seen.

Thus, it is concluded that radio-luminescence of water and ice itself, induced by α-particles, was measured. At least one of the transitions from the excited electronic states in each, water and ice, shows a temperature dependency. For further conclusions the emission spectra and decay kinetics have to be measured.

PoS(ICRC2017)1060

7. Luminescence yield

The luminescence yield was calculated from the rate of measured single photons which was cleaned from background and noise as described above. A Monte Carlo simulation was executed to estimate the number of emitted photons which can be seen by the PMT. The measured ice/water thickness, its distance to the PMT, the refraction at the ice/water - air surface and reflection at both, the gold layer of the source and the sample - air surface was calculated for each photon. The measured PMT spectral, and radial efficiency was also included. A uniform emission spectrum between 250 nm and 650 nm was assumed. The regarding uncertainty was included by assuming 100 nm wide peaks in this range. A more precise estimation requires the measurement of the emission spectrum and subsequent optical calibration.

The estimated luminescence yield for the given wavelength range is shown in Fig. 5. It ranges from $0.42^{+0.19}_{-0.25}$ γ/MeV to $0.50^{+0.23}_{-0.29}$ γ/MeV for water and from $0.54^{+0.64}_{-0.83}$ γ/MeV to $1.25^{+0.24}_{-0.31}$ γ/MeV for ice. A discontinuity between the measurements at 0 °C is expected due to the differences between electronic excitations in lattice and molecules in liquids. This result is in tension with two measurements of water luminescence [18] using distilled water which is usually of significantly lower purity than the water used in this study. The third measurement, which is within uncertainties in agreement with this result, is an in-situ measurement in the Baikal lake [11].

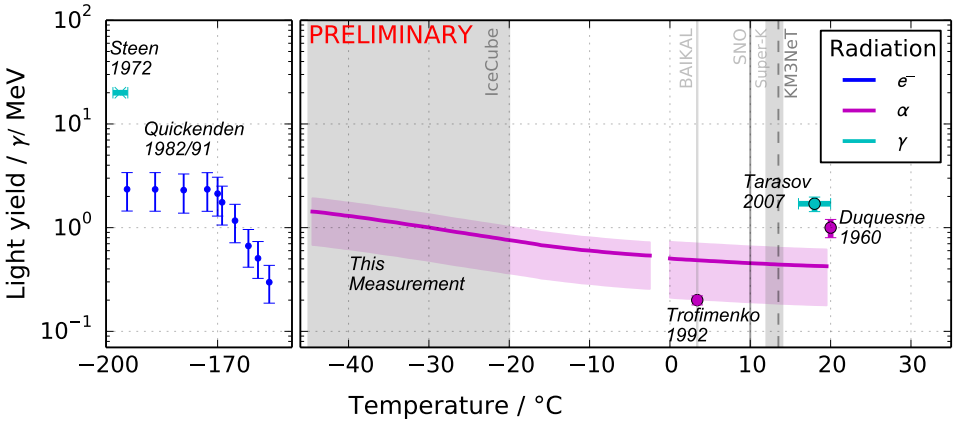


Figure 5: The result of this measurement is shown in comparison to measured luminescence yields of cold ice, warm ice, and liquid water induced by different kind of irradiations, taken from Refs. [2, 18, 19, 11]. Older measurements for cold ice are summarized in Ref. [2]. The water and ice temperatures of neutrino detectors are shown as vertical bands [9, 20]. In addition to the values above, there is a recent measurement of water luminescence induced by α-particles, protons, and carbon-ions which gives relative values only [21].

8. Summary and outlook

The luminescence of ice $> -45\,^{\circ}$C was measured for the first time. This opens up the prospect of using luminescence as a detection method for the IceCube neutrino telescope. It was shown in simulation studies that ice luminescence can be used for magnetic monopole detection if the

PoS(ICRC2017)1060

luminescence yield exceeds $0.2\,\gamma/\mathrm{MeV}$ [6] which is the case. However, the yield varies with ice temperature which is not constant through the depth of the detector volume.

The first measurement of the temperature dependence of water and ice ($)> -45\,^{\circ}\mathrm{C}$) luminescence was achieved. A temperature dependence was seen, however, this does not explain the tension between previous measurements. Further studies are planned to measure the influence of solubles to derive a value usable for neutrino detectors using liquid water as medium.

Further measurements are planned at ion accelerators to measure the emission spectra, decay kinetics and quenching behavior for a full characterization of water and ice luminescence. Water and ice samples from the detector sites will be used for these measurements in addition to ultra-purified water to take their properties into account.

References

[1] E. H. Belcher, *Proc. R. Soc. Lond. A* **216** (1953) 90–102.

[2] T. I. Quickenden, S. M. Trotman, and D. F. Sangster, *J. Chem. Phys.* **77** (1982) 3790.

[3] S. M. Trotman, T. I. Quickenden, and D. F. Sangster, *J. Chem. Phys.* **85** (1986) 2555.

[4] T. I. Quickenden et al., *J. Chem. Phys.* **95** (1991) 8843.

[5] V. Langford et al., *Acc. Chem. Res.* **33** (2000) 665–671.

[6] A. Pollmann. Proceedings of ICNFP'16. *arXiv:1610.06397*.

[7] P. Dirac, *Proc. Roy. Soc. A* **133** (1931) 60–73.

[8] Y. Hayato et al., *Phys. Rev. Lett.* **83** (1999) 1529.

[9] P. Bagley et al., *KM3NeT - Technical Design Report*, 2009. *http://inspirehep.net/record/1366114/files/TDRKM3NeT.pdf*.

[10] C. Xu et al., *J. Phys. Conf. Ser.* **718** (2016), no. 6 062070. ; B. Aharmim et al., *Phys. Rev. C* **72** (2005) 055502.

[11] V. Aynutdinov et al., *Astropart. Phys.* **29** (2008) 366 – 372. Original description in I. I. Trofimenko, preprint INR 765/92 (in Russian).

[12] M. S. Basunia, *Nuclear data sheets 107, 3323*, 2006.

[13] Photomultiplier Tube R1924P by HAMAMATSU Photonics K.K., 2017.

[14] PicoScope 6404B by Pico Technology, 2017.

[15] K. Helbing et al. AMANDA internal note IR/2030701.

[16] J. Beringer et al., *Phys. Rev. D* **86** (2012) 323. Ch. 30.

[17] E. Tamm and M. Frank, *Dokl. Akad. Nauk SSSR (Akad. of Science of the USSR)* **14** (1937) 107.

[18] M. Duquesne and I. Kaplan, *Phys. Radium* **21** (1960) 708. (in French); M. D. Tarasov et al., *Instrum. Exp. Tech.* **50** (2007), no. 6 761–763.

[19] H. B. Steen, O. I. Sorensen, and J. A. Holteng, *Int. J. Radiat. Phys. Chem.* **4** (1972) 75–86.

[20] A. Achterberg et al., *Astropart. Phys.* **26** (2006) 155–173. ; V. Aynutdinov et al., *Nucl. Instr. Meth. A* **602** (2009) 14–20. ; J. Boger et al., *Nucl. Instr. Meth. A* **449** (2000) 172–207. ; S. Fukuda et al., *Nucl. Instr. Meth. A* **501** (2003) 418–462.

[21] S. Yamamoto, in *Proc. SPIE*, vol. 10049. doi:10.1117/12.2255648.

PoS(ICRC2017)1060

PROCEEDINGS OF SCIENCE

Combined Search for Neutrinos from Dark Matter Annihilation in the Galactic Center using IceCube and ANTARES

The IceCube[†] and ANTARES Collaborations

[†]*http://icecube.wisc.edu/collaboration/authors/icrc17_icecube*

E-mail: juaguila@ulb.ac.be

Neutrino telescopes have searched for self-annihilating dark matter in the Galactic Halo and placed stern limits on the dark matter self-annihilation cross section $\langle\sigma v\rangle$ for dark matter particle masses above 30 TeV. To date, the most stringent limit were obtained by the ANTARES neutrino telescope looking at the Galactic Center region for masses > 100 GeV/c^2 and is closely followed by the limits of the IceCube experiment at lower masses. In this contribution, we present the sensitivities of a future combined search for dark matter in the Milky Way using data from both experiments. From the IceCube experiment, data from 2012 to 2015 with the complete 86-strings detector were selected, while from ANTARES the data sample collected from 2007 to 2015 have been used. The analysis considered dark matter with particle masses ranging from 50 to 1000 GeV/c^2. We used the annihilation into $\tau\bar{\tau}$ as a benchmark to explore the potential gain by combining the two experiments using a common likelihood framework.

Corresponding authors: J. A. Aguilar[*1], N. Iovine[1], C. Tönnis[2], J. D. Zornoza[3]

[1] *Université Libre de Bruxelles*

[2] *Sungkyunkwan University*

[3] *IFIC - Instituto de Física Corpuscular*

35th International Cosmic Ray Conference - ICRC217-
10-20 July, 2017
Bexco, Busan, Korea

[*]Speaker.

PoS(ICRC2017)911

1. Introduction

Astrophysical observations provide strong evidence for the existence of dark matter in the Universe, however its nature remains unknown. One of the most popular hypotheses for dark matter is that it is made up of non-baryonic particles called WIMP that are non-relativistic, electromagnetically neutral and interacting only via a weak interaction. According to observational evidence, the galaxies are embedded in a halo of thermal relic density of dark matter from the early Universe. The high density of dark matter particles at the center of galaxies, for example in our Milky Way, can contribute to the annihilation of WIMPs producing secondary particles such as high energy neutrinos.

Limits on WIMP dark matter annihilation cross-section have already been set by neutrino detectors such as IceCube [1] and ANTARES [2]. The purpose of this analysis is to combine the data of the two neutrino detectors in the form of probability density function of the two neutrino detectors for the search of neutrinos from dark matter annihilation in the Galactic Center (GC). Another goal of this work is to understand the differences in the approaches taken by Antares and IceCube for this kind of analysis.

2. The IceCube and ANTARES neutrino telescopes

Deep under-water/ice neutrino telescopes follow a similar detection principle. Given the low interaction cross-section of neutrinos, a large volume of target material is required which is achieved by placing a sparse array of photodetectors in deep, dark, and transparent environments such as the sea or the Antarctic ice. The photodetectors will record the Cherenkov emission induced by the secondary particles produced in the deep-inelastic scattering (DIS) interaction of a neutrino with a nucleon of the surrounding medium. The main objective of neutrino telescopes is the detection of astrophysical neutrinos produced close to the cosmic ray sources. However, given the versatility of these experiments they can be used to search for dark matter signatures in an indirect fashion.

The main background contribution of neutrino telescopes comes from atmospheric muons and atmospheric neutrinos. These particles are produced by the interaction of cosmic rays with the higher layers of our atmosphere. Atmospheric muons trigger the detectors more than 6 orders of magnitude more often than atmospheric neutrinos. For up-going directions, the Earth acts as a shield against atmospheric muons. As a consequence, declination corresponding to angles between $0^\circ - 90^\circ$ are less background dominated in the IceCube detector. For ANTARES, declination below -47° are less background dominated since they are always below the horizon of the detector. Declination between -47° and 47° are below the horizon for part of the sidereal day.

2.1 IceCube

IceCube is a cubic-kilometer neutrino observatory located at the South Pole [3] between depths of 1,450 m and 2,450 m and was completed in 2010. The IceCube observatory consists of an array of 5,160 digital optical modules (DOMs) attached to vertical strings placed in 86 boreholes. The reconstruction of the direction, energy and flavor of the neutrinos relies on the optical detection of Cherenkov radiation emitted by charged particles produced in the interactions of neutrinos in the

PoS(ICRC2017)911

surrounding ice or the nearby bedrock. In the center of the detector, eight strings are deployed in a more compact way, forming the DeepCore subdetector. This denser configuration extends the detection of neutrinos to energies below 100 GeV.

For this analysis, we use the IceCube data selection developed in the course of the Galactic Center WIMP search analysis [4]. This data sample consists of 1007 days of track-like events compatible with ν_μ signatures taken with the 86-strings configuration from the 15th of May 2012 to 18th of May 2015. Being located at the South Pole, IceCube observes the Galactic Center in the Southern Hemisphere where the background is dominated by atmospheric muons. The selection uses a veto-technique to reduce the level of atmospheric muons by seven orders of magnitude. Details of the event selection can be found in [4]. The total number of events in our sample is 22,553 events.

2.2 ANTARES

The ANTARES telescope is an underwater Cherenkov detector located in the Mediterranean sea, about 40 km from Toulon at depth of roughly 2500 m [5]. ANTARES is a smaller array consisting of 885 optical modules (OM) placed along 12 lines of 350 meters each, spread over a surface of 0.1 km^2 on the seabed and kept vertical by buoys located at their top. In this work, we consider a data sample corresponding to a total lifetime of 2101.6 days, which corresponds to the actual ANTARES uptime from 2007 to 2015 [6]. The ANTARES detector uses two different reconstruction algorithms depending on the deposited energy of the events: a single line reconstruction for events below 100 GeV and multi-line reconstruction for energies over 100 GeV. The total number of events in this sample is 595 events. Despite its smaller scale compared to IceCube, ANTARES has a privileged view of the Galactic Center as it can use the Earth to block the main contribution of the atmospheric background and therefore no veto is necessary.

3. Dark Matter Annihilation Flux

The expected neutrino flux to be observed in neutrino telescopes from dark matter annihilation is given by [7]

$$\frac{\mathrm{d}\phi_\nu(\Psi)}{\mathrm{d}A\,\mathrm{d}\Omega\,\mathrm{d}t\,\mathrm{d}E} = \frac{\langle\sigma_A v\rangle}{2}\,\frac{J_a(\Psi)}{4\pi m_\chi^2}\,\frac{\mathrm{d}N_\nu}{\mathrm{d}E}\,, \tag{3.1}$$

where m_χ is the mass of the WIMP, $\langle\sigma_A v\rangle$ is the WIMPs thermally-averaged annihilation cross-section and $\mathrm{d}N_\nu/\mathrm{d}E$ is the neutrino energy spectrum per annihilating WIMP pair. $J_a(\Psi)$ is the integrated J-factor defined as the integral of the squared dark matter density along the line-of-sight

$$J_a(\Psi) = \int_0^{l_{max}} \rho_\chi^2\left(\sqrt{R_{sc}^2 - 2\,l\,R_{sc}\,cos(\Psi) + l^2}\right)\mathrm{d}l\,, \tag{3.2}$$

where Ψ denotes the opening angle to the Galactic Center, R_{sc} is the radius of the solar circle ($R_s \simeq 8.5$ kpc), and ρ_χ is the dark matter density profile. The quantity l is the distance along the line-of-sight and the upper integration limit l_{max} is a quantity which depends on the radius of the Galactic Halo R_{halo} and can be expressed as

PoS(ICRC2017)911

$$l_{max} = \sqrt{R_{halo}^2 - sin^2\Psi R_{sc}^2} + R_{sc}\, cos\Psi \,. \tag{3.3}$$

The radius of the Galactic Halo is chosen to be the radius of the Milky Way $R_{halo} = 50$ kpc and Ψ is the angular distance from the Galactic Center. For this analysis, we used the Navarro-Frenk-White (NFW) dark matter profile

$$\rho_\chi(r) = \frac{\rho_0}{\frac{r}{r_s}(1+\frac{r}{r_s})^2} \,, \tag{3.4}$$

where the parameters to model the matter distribution in the Milky Way are defined in [8], with r_s being the scale radius and ρ_0 the characteristic dark matter density. From these ingredients, it is possible to derive the astrophysical J-factor as a function of Ψ, which is shown in fig. 1 (left).

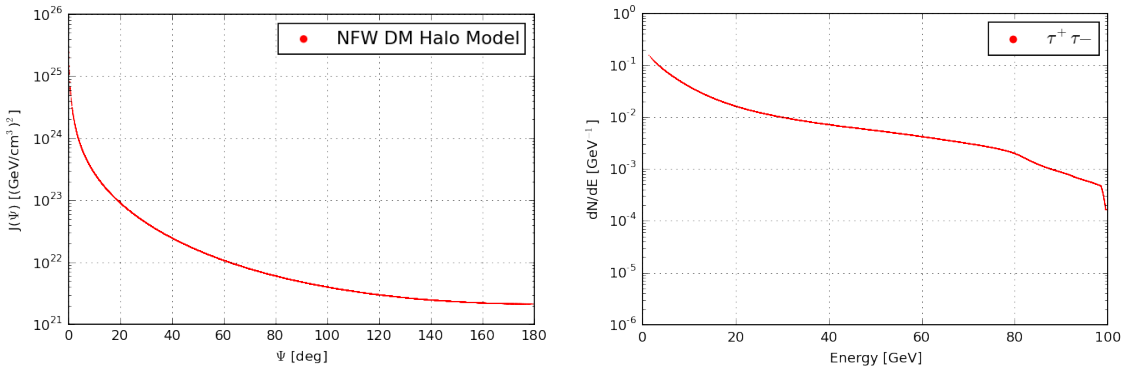


Figure 1: Left: J-factor as a function of the opening angle Ψ calculated for the NFW halo model with the parametrisation found in [8]. **Right :** Neutrino energy spectrum at Earth for the annihilation of WIMP particle of 100 GeV/c^2 mass with ν_μ in the final state through the $\tau\bar{\tau}$ annihilation channels.

In the following paragraphs, we will focus on the decay of WIMP particles via the $\tau\bar{\tau}$ annihilation channel as a benchmark of the analysis for WIMP masses ranging from 50 GeV/c^2 to 1000 GeV/c^2 where the sensitivity of both experiments is comparable. At higher masses, the ANTARES telescope dominates since the effective volume scales with the range of the resulting muon, while the veto-technique of IceCube is beneficial at lower masses. A 100% branching ratio into the $\tau^+\tau^-$ decay channel is assumed. The average neutrino spectra per annihilation process (dN/dE) for these masses and $\tau^+\tau^-$ decay channel were computed using PYTHIA simulation package [9] and are shown in Fig.1 (right).

4. Analysis Method

A binned maximum likelihood method with the two-component mixture model is performed for all annihilation channels assuming WIMP masses ranging from 50 to 1000 GeV/c^2. The first step is to determine the probability density functions (PDFs) of the signal as well as of the background for each experiment. For IceCube, the PDFs used consist of 2-dimensional distributions in right ascension and declination. IceCube PDFs use 12 bins for a band covering [-2, 2] radians

PoS(ICRC2017)911

in declination and 10 bins in the full range of right ascension [-2π, 2π] (see Fig.2). As already mentioned, at low masses ANTARES only reconstructs events using single-line events where the azimuth estimate is not possible. For WIMP masses between 500 and 1000 GeV/c^2, the multiline reconstruction was used. In both case, PDFs are 1-dimensional distributions of the opening angle Ψ with respect to the Galactic Center (see Fig. 3). The idea of the likelihood analysis is to compare the data to the shapes of the expected signal and the background.

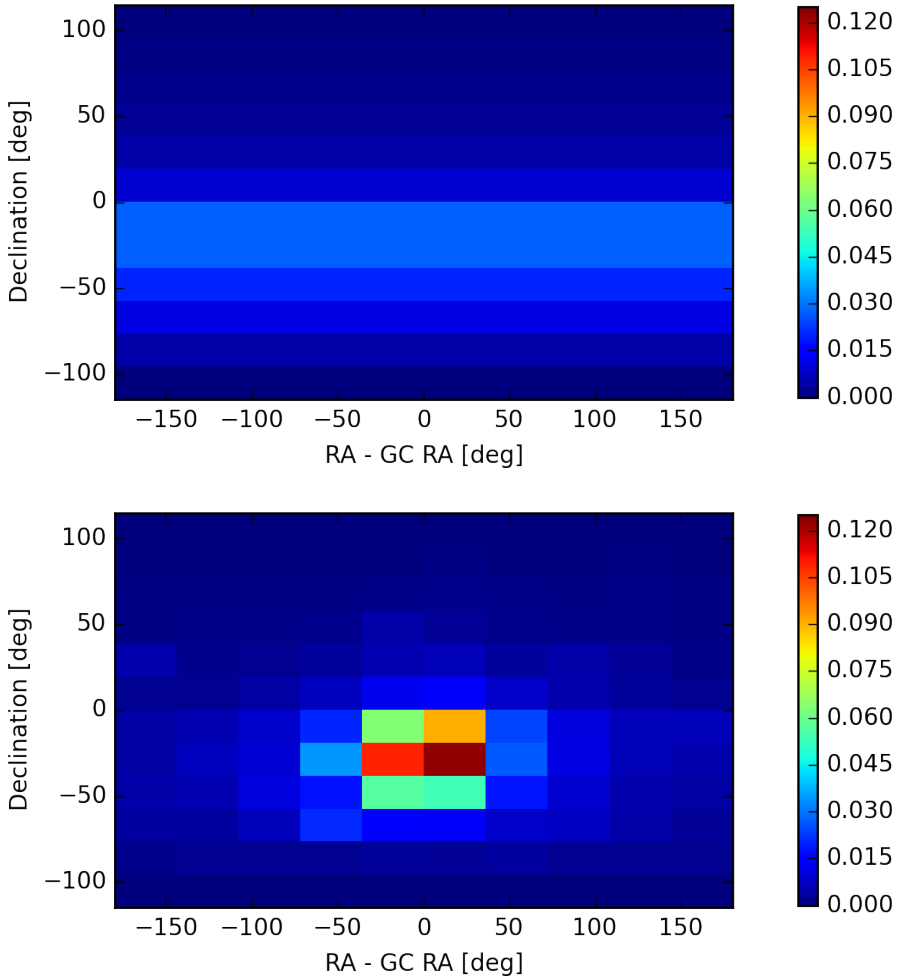


Figure 2: Top: Normalized background PDF of the IceCube sample. Bottom: Normalized signal PDF for the annihilation of 100 GeV/c^2 WIMP particle into the $\tau^+\tau^-$ channel.

The binned likelihood method used in this analysis is defined as

$$\mathscr{L}(\mu) = \prod_{bin_i=bin_{min}}^{bin_{max}} \text{Poisson}\left(n_{obs}(bin_i)|n_{obs}^{tot} f(bin_i|\mu)\right) , \tag{4.1}$$

where the parameter to minimize, μ, is the ratio of the number of signal events over the total number of background events in the sample n_{obs}^{tot}. The method compares the observed number of events in a given bin i, $n_{obs}(bin_i)$, with the expectations, n_{obs}^{tot}, $f(bin_i|\mu)$, where

PoS(ICRC2017)911

$$f(bin_i|\mu) = \mu\, f_s(bin_i) + (1-\mu)\, f_{bg}\ , \tag{4.2}$$

is the fraction of events in the bin i, with f_s and f_{bg} being the signal and the background density distributions shown in Fig. 2 and Fig. 3. In the case of a combined analysis, two likelihoods are combined in a single $\mathscr{L}_{comb}(\mu)$ defined as

$$\mathscr{L}_{comb}(\mu) = \prod_{k=0}^{2} \mathscr{L}_k(\mu_k)\ , \tag{4.3}$$

where $k = 0$ represents the ANTARES likelihood and $k = 1$ the IceCube likelihood. Each detector has a signal to background ratio given by $\mu_k = w_k\mu$ where the weight w_k is calculated by taking into account the relative expected number of signal events in each detector, and the relative number of background events in each sample.

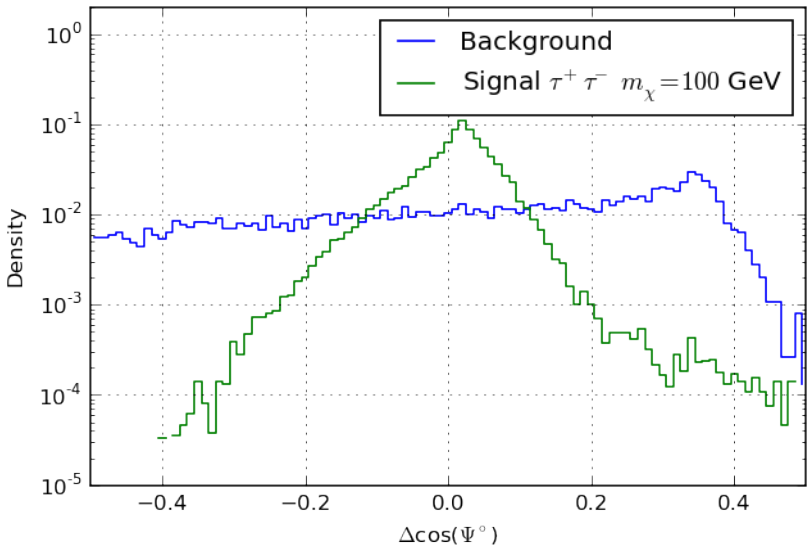


Figure 3: The blue line shows the normalised background PDF of the ANTARES sample, while the green line is the normalised signal PDF for WIMP particles of 100 GeV/c^2 mass that annihilate into via the $\tau^+\tau^-$ channel.

The best estimate of the signal fraction is obtained by minimizing $-\log\mathscr{L}_{comb}(\mu)$. If this value is consistent with zero, the upper limit on the signal fraction, $\mu_{90\%}$, is estimated by determining the 90% confidence interval using the Feldman-Cousins approach [10]. The signal fraction can be linked to $\langle\sigma_A v\rangle$ using the estimated number of signal events for the specific dark matter signal (mass, channel and halo profile). The upper limit on $\langle\sigma_A v\rangle$ for background events only is then calculated by generating a pseudo-experiments sample of 100,000 events and by determining the p-value for the value μ found in the data. We chose to quote the sensitivity as the median value of the 90% upper limits obtained.

PoS(ICRC2017)911

5. Results and discussion

The sensitivity to $\langle \sigma_A \nu \rangle$ for the combined analysis of IceCube and ANTARES is shown in Fig.4. The results show an improvement of the sensitivity in the energy range of 65 to 1000 GeV/c^2 when compared to the individual results of both IceCube and ANTARES. This analysis opens the possibility to explore additional channels ($b\bar{b}$, W^+W^-, $\nu_\mu\nu_\mu$, $\mu\bar{\mu}$ and $\tau\bar{\tau}$) and halo profiles in order to set the best limits for a combination of results from all neutrino telescopes.

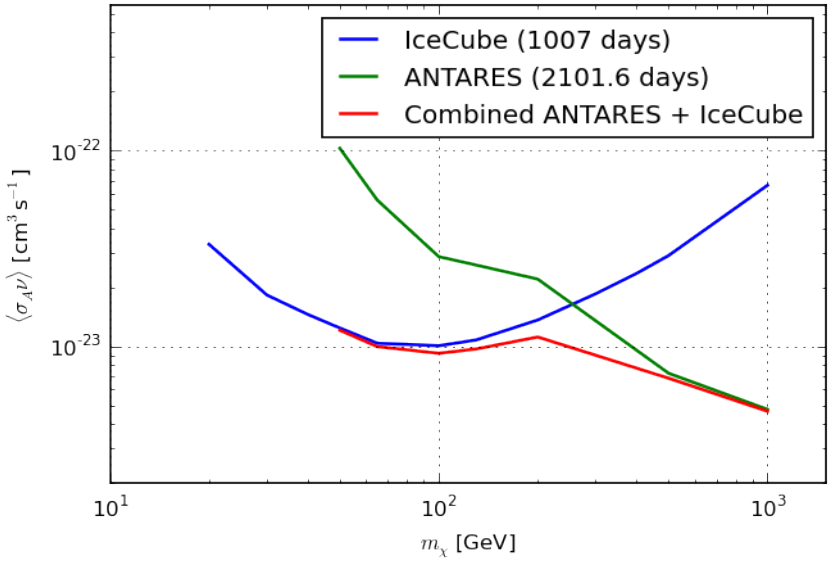


Figure 4: Preliminary plot of the sensitivities obtained for 2101.6 days of ANTARES data (green), 1007 days of IceCube data (blue) and the combination of both experiment (red).

References

[1] **IceCube** Collaboration, M.G. Aartsen et al., *EPJ* **C75** (2015) 10, 492.

[2] **ANTARES** Collaboration, S. Adrian et al., *J. Cosmol. Astropart. Phys.* **10** (2015) 068.

[3] **IceCube** Collaboration, M.G. Aartsen et al., *JINST* **12** (2017) P03012.

[4] **IceCube** Collaboration, M.G. Aartsen et al., `hep-ex/1705.08103`.

[5] **ANTARES** Collaboration, M. Ageron et al., *Nuclear Instruments and Methods in Physics Research Section A: Accelerators, Spectrometers, Detectors and Associated Equipment* **656** (2011) 011.

[6] **ANTARES** Collaboration, A. Albert et al., *Physics Letters B* **769** (2017) 249.

[7] H. Yüksel, S. Horiuchi, J. F. Beacom, and S. Ando *Physical Review D* **769** (2017) 249.

[8] F. Nesti, P. Salucci, *JCAP* **07** (2013) 016.

[9] T. Sjöstrand, S. Mrenna, and P. Skand, *JHEP* **05** (2006) 026.

[10] G.J. Feldman, R.D. Cousins, *Phys.Rev.* **D57** (1998).

PoS(ICRC2017)911